THESIS

CLOUD PROPERTY RETRIEVALS USING POLARIMETRIC RADAR: UNTANGLING SIGNALS OF PRISTINE ICE AND SNOW

Submitted by

Nicholas J. Kedzuf

Department of Atmospheric Science

In partial fulfillment of the requirements

For the Degree of Master of Science

Colorado State University

Fort Collins, Colorado

Fall 2020

Master's Committee:

Advisor: J. Christine Chiu

Peter Jan van Leeuwen
Paul DeMott
V. Chandrasekar

ABSTRACT

CLOUD PROPERTY RETRIEVALS USING POLARIMETRIC RADAR: UNTANGLING SIGNALS OF PRISTINE ICE AND SNOW

Ice and mixed phase clouds are critical components of Earth's climate system via their strong controls on global precipitation distribution and radiation budget. Their microphysical properties have been characterized commonly by polarimetric radar measurements. However, there remains a lack of robust estimates of ice number concentration, due to the difficulty in distinguishing embedded pristine ice from snow aggregates in remote sensing observations. This hinders our ability to study detailed cloud ice microphysical processes from observations.

This thesis presents a rigorous method that separates the scattering signals of pristine ice and snow aggregates in scanning polarimetric radar observations to retrieve their respective abundances and sizes for the first time. This method, dubbed ENCORE-ICE, is built on an iterative ensemble retrieval framework. It provides number concentration, median volume diameter, and ice water content of pristine ice and snow aggregates with full error statistics. The retrieved cloud properties are evaluated against in-situ aircraft measurements from a UK field campaign. For a stratiform cloud system with embedded convective features associated with observed ice number concentration of 0.1–10 L^{-1} and ice water content from 0.01–0.6 g m^{-3}, the retrievals are mainly in the range of 1.0 –15 L^{-1} and 0.003–0.6 g m^{-3}.

To investigate the ice property evolution in a Lagrangian sense, the retrieval method is also applied to along-wind scanning radar measurements from an Atmospheric Radiation Measurement (ARM) campaign in Finland. For the cases presented, snow aggregates are

typically of 5–10 mm size in diameter, which is ~10 times larger than pristine ice and thus dominates radar reflectivity. However, the partitioning in ice water content between pristine ice and aggregates varies and largely depends on ice number concentration. More importantly, the retrieved pristine ice number concentration exceeds the predicted concentration of primary ice nuclei at a mid-cloud temperature of –15°C by two orders of magnitude, suggesting possible secondary ice production, one of the outstanding issues in cloud physics. This highlights the potential of using ENCORE-ICE to identify secondary ice production events and understand their trigger mechanisms.

ACKNOWLEDGEMENTS

This work would not be possible without the guidance and support from countless people in various capacities. Most paramount of this cohort is my advisor, Dr. Christine Chiu. On paper, I was not the strongest candidate for joining her group. Nonetheless, she recognized potential and was willing to take a chance. Over the last 2.5 years, she has provided countless hours of advice on sound research tactics, teaching, networking and professionalism, work-life balance, and much more. She is a champion of our work and has spent far more time and energy than warranted picking my head up when I was feeling discouraged. Her foremost lesson is that time is never wasted and no effort is in vain, so long as you learn from the experience. Her efforts have been, and will continue to be, instrumental in molding me into the strongest scientist I can be. For all of the above, I am eternally grateful.

Secondly, I would like to thank my committee members: Drs. V. Chandrasekar, Paul DeMott, and Peter Jan van Leeuwen. Over the course of the project, Dr. Chandrasekar has provided indispensable knowledge and intuition regarding polarimetric radar analysis. My knowledge base would be nowhere near its current state without his input. Similarly, Dr. DeMott has provided invaluable guidance on ice nucleation processes, aerosol physics, and aerosol data processing. Dr. van Leeuwen markedly enhanced my understanding of theory and best practices when implementing an ensemble Kalman filter framework. Each were extremely inviting and gentle with someone who previously had little to no understanding of their respective expertise.

Thirdly, the following have contributed in some way to this work and the publication in preparation: Sounak Biswas, Shashank Joshil, Dr. Yinghui Lu, Dr. Chris Westbrook, Dr. Yann Blanchard, Dr. Bradley Isom, Dr. Nitin Bharadwaj, and Dr. Brenda Dolan. Without each of their

unique and critical contributions, this work would not have come to fruition. I would also like to thank Dr. Sonia Kreidenweis for contributing her extensive knowledge on aerosol physics and aerosol data processing.

Lastly, I would like to thank my family, friends, and community within the Department of Atmospheric Science at Colorado State University. To my parents, Debra and Joseph and my siblings, Leah and J.P.: thank you all for your undying support and genuine effort to better understand what it is I do. You have tolerated numerous instances of "but I really need to work" when home visiting or planning to visit and a good deal of complaining over the phone. To my dog, Juneau: thank you for perennially looking at me like I am a Nobel laureate, regardless of the quality of my science or dedication on any given day. To my housemates over the past year; Adam Clayton, Matthew Lang, and Jeremiah Piersante: thank you for the support, late night venting sessions, and for sticking together during quarantine and the beginnings of work-from-home. I would also like to thank Sarah Tisdale and all other members of the Department of Atmospheric Science front office for their consistent support with logistics from my acceptance into the department through the completion of my degree.

I would also not be here without monetary support. This work is supported by the Office of Science (BER), Department of Energy under grants DE-SC0018930.

TABLE OF CONTENTS

LIST OF TABLES

LIST OF FIGURES

CHAPTER 1

Introduction

Clouds cover approximately two thirds of our planet (Mace et al. 2009) and are critical components of Earth's climate system (Stephens et al. 2005) on timescales ranging from days to decades. Their spatiotemporal variability is largely responsible for the redistribution of liquid water throughout the land-ocean-atmosphere system via precipitation, or lack thereof (Boucher et al. 2013). They are also critical components in earth's radiative budget (Stephens et al. 2012), because they reflect solar shortwave radiation back to space and absorb and emit terrestrial longwave radiation. These radiative interactions lead to dueling cooling and warming effects, respectively, which have proven difficult to quantify due to their intricate dependence on cloud properties (Baran 2009). As such, clouds remain a dominant source of uncertainty in future climate projections (Boucher et al. 2013).

This uncertainty stems from the sheer number and complexity of processes acting within, and adjacent to, a cloud. These processes operate and interact on spatial scales from micrometers to kilometers, temporal scales from seconds to hours, and involve the simultaneous cycling (and recycling) of cloud water between gas, liquid, and ice phases. Clouds are comprised of liquid water at temperatures warmer than 0°C and ice at temperatures colder than approximately –38°C (Cantrell and Heymsfield 2005). However, between 0°C and –38°C, clouds can exist as both liquid and ice (hereafter referred to as mixed-phase clouds) and are often characterized by interactions between ice and supercooled liquid water.

This thesis will focus on clouds containing ice, whether they be purely ice phase or mixed-phase clouds. Ice clouds are responsible for the majority of precipitation globally, and even greater proportions (80–90%) in the midlatitudes and polar regions (Field and Heymsfield 2015). Yet, relative to liquid clouds, many of the fundamental microphysical processes governing the evolution of ice and mixed-phase clouds remain poorly understood and poorly represented in numerical models (Boucher et al. 2013). This is partly due to a lack of global observational constraints on ice cloud properties such as cloud ice number concentration (Sourdeval et al. 2018). In contrast to liquid cloud properties such as droplet number concentration and liquid water content, cloud ice number concentration is difficult to quantify remotely because it is not directly related to other commonly retrieved cloud properties such as optical depth or hydrometeor effective radius (Sourdeval et al. 2018). This lack of direct mapping is a function of the tremendous range of ice crystal shapes and sizes (Bailey and Hallett 2009), dictated by further complex ice nucleation and growth processes which depend on atmospheric conditions such as temperature, moisture, and vertical velocity (Tiira and Moisseev 2020).

For clouds with temperatures warmer than –38°C (the focus of this study), aerosol particles known as ice nucleating particles (INPs) are required for ice to nucleate (Kanji et al. 2017). INPs lower the energy barrier required for formation of the initial ice embryo, known as heterogenous ice nucleation, which would be otherwise thermodynamically unfavorable at such temperatures (Kanji et al. 2017). Immersion freezing, by which an INP enters a liquid cloud droplet and enables freezing once lofted to sufficiently cold temperatures, is thought to be the most relevant heterogenous ice nucleation mode for mixed-phase clouds (e.g. Westbrook and Illingworth 2013). Ice formation in such clouds is thus directly related to the numerous types and

extremely heterogenous distributions (orders of magnitude variation globally) of aerosol particles present (Yun and Penner 2012). Yet, despite considerable progress on the subject in decades past, aspects of heterogenous nucleation remain mysterious (DeMott et al. 2010). This due in part to the reduced correlation between aerosol concentrations and cloud ice number concentration over time in the presence of additional ice formation processes such as secondary ice production (SIP), ice growth processes such as aggregation and riming, and the redistribution of ice from other regions in the cloud (DeMott et al. 2011).

SIP processes are similarly poorly understood and difficult to observe, yet can lead to rapid increases in ice number concentration that can impart large forcing on cloud radiative and precipitation properties (Field et al. 2017). However, for SIP to occur, some amount of ice must have already formed via primary formation mechanisms and exist in atmospheric conditions that support SIP. Necessary and sufficient preexisting ice number concentrations and atmospheric conditions supportive of SIP are also poorly understood (Field et al. 2017). This intricate relationship between primary and secondary ice formation mechanisms further solidifies the importance of understanding primary ice formation mechanisms. Overarchingly, it is critical that the community understand processes governing the abundance of ice particles in clouds, because the relative partitioning of cloud water between ice and liquid phases impacts a cloud's radiative properties (Fusina et al. 2007) as well as its precipitation efficiency and lifetime (Lindsey and Fromm 2008). Ice growth processes such as aggregation and riming are also strong controls on precipitation production and cloud lifetime because they enhance particle mass and fall speed (Gultepe et al. 2017).

While considerable knowledge has been gleaned from laboratory and modelling studies, both settings do not, and currently cannot, capture the full complexity of ice microphysical

processes and their interactions in a cloud. Therefore, process-driven observational studies are critical for documenting the variability and evolution of these processes and to better inform their representation in numerical models. Such observational platforms include in-situ (i.e. aircraft) and remote sensing platforms like ground-based radar/lidar and earth-observing satellites. While aircraft can document cloud microphysical properties at high spatiotemporal resolution, they are not an ideal observing platform for holistically capturing microphysical process evolution due to their limited sampling volumes (Korolev et al. 2017; Gryspeerdt et al. 2018). Earth-observing satellites can characterize cloud microphysical properties on much larger spatiotemporal scales than aircraft or ground-based platforms, but are still limited to a temporal snapshot that is insufficient for characterizing process evolution at sub-cloud scale. Furthermore, satellite-based observing methods typically focus on the ice properties of high clouds at temperature colder than –30°C (e.g. Sourdeval et al. 2018) and are optimized for such conditions. Ground-based polarimetric radar, on the other hand, can contiguously document cloud evolution with spatial resolutions of hundreds of meters or less and temporal resolutions on the order of seconds for extended periods of time. These characteristics make ground-based polarimetric radar an ideal candidate for documenting the Lagrangian evolution of ice microphysical properties and how this translates to changes in cloud evolution.

Polarimetric radar can provide information on ice particle size, concentration, fall speed, and orientation through its near-simultaneous measurement of horizontally and vertically backscattered power. Consequently, it has long been used to qualitatively identify “fingerprints” of ice growth processes such as vapor deposition (e.g. Kennedy and Rutledge 2011), riming (e.g. Grazioli et al. 2015), and snow aggregation (e.g. Moisseev et al. 2015). However, a longstanding hurdle in polarimetric studies of ice microphysics is an inability to separate and quantitively

interpret the individual contributions to the cumulative polarimetric radar signal from different ice hydrometeor species (Magono 1962) because of their diverse scattering properties (Bringi and Chandrasekar 2005). For example: larger, pseudo-spheroidal snow aggregates that tumble as they fall often dominate the radar signal (Hogan et al. 2002) and thus mask contributions associated with smaller, preferentially oriented, high aspect ratio pristine ice crystals (Keat and Westbrook 2017). Information from one polarimetric variable alone, such as the total backscattered power (horizontal reflectivity; Z_{H}), is insufficient to characterize such mixtures of ice hydrometeors (Oue et al. 2018). This inability to isolate their respective signals has limited the amount of progress towards retrieving the explicit number concentration of pristine ice from polarimetric radar.

However, greater insight is possible when multiple polarimetric variables are used in concert. Such approaches have been used to estimate cloud ice number concentration and other bulk ice microphysical properties. Murphy et al. (2020) used empirical relationships between Z_{H}, the difference between horizontal and vertical reflectivities (Z_{DP}), differential reflectivity (Z_{DR}), and specific differential phase shift (K_{DP}) to estimate ice water content (IWC, denoted as q_I), ice number concentration (N), and particle median volume diameter (D_0). However, these polarimetric relationships, developed by Ryzhkov et al. (2018), are for bulk properties and do not enable the separation of contributions from pristine ice and snow aggregates. Spek and Unal (2007) developed a nonlinear least-squares optimization approach for retrieving particle size distribution (PSD) parameters of pristine ice crystals and snow aggregates from the spectral forms of Z_{H} and Z_{DR} by exploiting the distinct differences in their fall behaviors. Schrom and Kumjian (2015) married Z_{H}, Z_{DR}, and K_{DP} to similarly estimate the PSD parameters of pristine ice crystals in the dendritic growth zone of Colorado winter storms. Keat and Westbrook (2017)

also demonstrated that it is possible to estimate the relative radar signal contributions of pristine ice crystals using Z_{H}, Z_{DR}, and copolar correlation coefficient (ρ_{HV}). However, these methods either fail to account for the complex morphologies of snow aggregates (e.g. Spek and Unal 2007), make a priori assumptions about the scattering contributions of snow aggregates (e.g. Schrom and Kumjian 2015; Keat and Westbrook 2017), or are limited to temperatures colder than –10°C to –15°C (Ryzhkov et al. 2018; Murphy et al. 2020).

Here, a novel framework is presented for simultaneously retrieving the respective N and q_I of pristine ice crystals and snow aggregates using polarimetric radar observations by adapting the ENsemble ClOud REtrieval method (ENCORE) developed by Fielding et al. (2014; 2015). Our version, adapted for the retrieval of ice cloud properties, is hereafter referred to as ENCORE-ICE. Using a database of ice crystal scattering properties (Lu et al. 2016) produced from realistic scattering models of pristine ice crystals and snow aggregates, the contributions to the radar signal from each hydrometeor species can be simulated. It is subsequently possible to retrieve their respective N and q_I without making assumptions about their relative contributions to the total polarimetric signal, an advance previously thought to be impossible. This thesis intends to answer two science questions. Firstly, is the set of polarimetric observables used here sufficient to explicitly characterize the contributions of pristine ice and snow aggregates to the radar signal and use this information to deduce their respective N and q_I? Secondly, what novel information can be gained about atmospheric controls on ice microphysical processes through implementation of this retrieval framework; with particular emphasis on primary ice nucleation, the transition to aggregation, and SIP processes.

The suite of polarimetric radar moments and the unique information each contributes to make this retrieval possible is first introduced in Section 2.1, along with a description of the

polarimetric datasets employed in this study. Section 2.2 outlines complementary datasets used to enhance the information gleaned from our retrieval framework. The structure of ENCORE-ICE and its components, along with practical considerations for implementation, are discussed in Chapter 3. Section 4.1 compares retrieval case studies from Chilbolton, United Kingdom against collocated in-situ aircraft observations as a means of evaluation. Section 4.2 discusses retrieval case studies from Hyytiälä, Finland and presents a methodology for assessing the Lagrangian time rate of change of N and q_I and incorporates estimates of primary ice number concentration to assess the possibility of SIP. Lastly, Chapter 5 poses final conclusions and establishes a roadmap to future insights of ice and mixed-phase cloud processes using the retrieval framework that is described here.

CHAPTER 2

Data

2.1 Polarimetric radar data

Our retrieval method uses four polarimetric observables. The first observable is the horizontally backscattered power (horizontal reflectivity; Z_{H}), which provides information on particle size since it is proportional to the sixth moment of the particle size distribution (PSD). As such, Z_{H} is dominated by contributions from snow aggregates, rimed particles, and/or graupel because their maximum dimensions, and thus their backscatter cross-sections, are typically much larger than those of pristine ice crystals. The second observable is the log-ratio of horizontally and vertically backscattered power (differential reflectivity, Z_{DR}), which provides information on particle shape and orientation. A Z_{DR} of 0 dB indicates spherical particles because of equal backscattered power in each polarization. Snow aggregates yield low Z_{DR} (0–0.6 dB), due to their spheroidal morphology and tumbling fall behavior. In contrast, pristine ice particles can yield Z_{DR} of several dB because of their aspect ratios and preferential horizontal orientation when falling. As Z_{DR} is reflectivity-weighted, heterogenous regions of pristine ice crystals and snow aggregates are therefore associated with lower Z_{DR} than if the snow aggregates were not present.

The third observable is the copolar correlation coefficient between horizontally and vertically backscattered power (ρ_{HV}), which provides information on the diversity of particle shape in a radar sample volume (Kumjian 2013; Keat et al. 2016). ρ_{HV} is unity in homogenous regions but tends towards lower values (~0.95) in the presence of heterogenous hydrometeor

types. Finally, the fourth observable is the specific differential phase shift (K_{DP}), defined as one half the range derivative of the differential phase shift (ϕ_{DP}). K_{DP} provides information on particle N, aspect ratio, and orientation. K_{DP} is fundamental to this framework because it is much more sensitive to pristine ice crystals and is not dampened by the presence of snow aggregates, unlike Z_{DR}. Compared to the first two observables that have been used in many remote sensing applications, the measurements of ρ_{HV} and K_{DP} are more advanced and their applications remain to be explored.

We use polarimetric radar data from two field campaigns to accomplish different yet complementary goals. The first goal is to evaluate our retrieval against in-situ measurements, using data from the Parameterizing Ice Clouds using Airborne obServationS and triple-frequency dOppler radar data (PICASSO) field campaign in Chilbolton, UK in 2018–2019. During the campaign, the National Centre for Atmospheric Science mobile X-band dual-polarization Doppler weather radar (NCAS NXPol; Neely III et al. 2018) had a 0.98° beam width and was configured to operate at 150 m range resolution with a maximum range of 150 km. The radar performed half-hemispheric (0°–90°) fixed-azimuth range-height indicator (RHI) scans at a rate of 5° s^{-1}, completing each scan in 18 s. Due to data availability, only data from 13 February 2018 are used. Throughout the day, 255 RHI scans were performed and were intercepted by NCAS-managed Facility for Airborne Atmospheric Measurements (FAAM) aircraft transects along the 243° radial on several occasions, providing a unique opportunity for evaluations.

The second goal is to demonstrate case studies for the evolution of ice microphysical processes, using polarimetric radar data from the Biogenic Aerosols – Effects on Clouds and Climate (BAECC) field campaign, an Atmospheric Radiation Measurement (ARM) program Mobile Facility deployment in Hyytiälä, Finland from January–September 2014 (Petäjä et al.

2016). While several radars operated during this campaign, we focus on data from the ARM X-band scanning cloud radar (XSACR; Kollias et al. 2014), due to the availability of the four observables mentioned above. In contrast to NXPol, XSACR has a wider beam width of 1.27° and a shorter maximum range of 25 km. However, XSACR has finer range resolution of 25 m and faster scan rate of 9° s^{-1}. For further comparison, characteristics of NXPol and XSACR are summarized in Table 2.1.

Table 2.1 Technical characteristics of the XSACR and NXPol polarimetric radars. For further specifications and more detailed descriptions of the radar systems, see Kollias et al. (2014) and Neely III et al. (2018), respectively.

Parameter	XSACR	NXPol
Center wavelength (mm)	30.81	31.98
Transmit/receive polarization	H+V/H+V	H+V/H+V
Beamwidth (°)	1.27	0.98
Pulse width (μs)	0.33	1
Scan rate (° s^{-1})	9.8	5
Sensitivity (dBZ)	–5 (5 km)	–11 (100 km)
Maximum range (km)	25	150
Gate Resolution (m)	25	150

During BAECC, XSACR predominantly performed hemispheric (0°–180°) RHI scans. The scans largely alternated between fixed-azimuth along-wind (AWRHI) and crosswind scan configurations. We focus on the XSACR AWRHI scans, because they provide the opportunity to

document the spatiotemporal evolution of ice microphysical processes in-cloud as the cloud field advects past the radar site. Over the course of the campaign, approximately 18 scan periods were performed per day. Each scan period lasted 20–25 minutes and is comprised of 60–70 hemispheric sweeps. These scan periods were often performed back-to-back, yielding 40–50 minutes of continuous AWRHI observations. This combination of high temporal resolution and sufficiently long observing period is well suited to capture ice microphysical evolution, including relatively rapid processes such as aggregation and SIP, as well as slower processes like pristine ice growth via vapor deposition.

All radar data underwent a series of quality checks and corrections before being used for retrieval. Z_{H} and Z_{DR} were corrected for attenuation due to liquid water, using the ϕ_{DP} method described in Bringi and Chandrasekar (2005). We ignore attenuation due to ice, because it is negligible at X-band (Vivekanandan et al. 1999). Systematic biases in Z_{DR} were identified using zenith-pointing Z_{DR} observations. As hydrometeors produce Z_{DR} of 0 dB when viewed at zenith due to their spherical symmetry (e.g. raindrops) or lack of preferential azimuthal orientation (e.g. ice particles), any residual Z_{DR} can be treated as bias and removed (Seliga 1981). For NXPol, a Z_{DR} correction factor of 0.2 dB is used. The two XSACR cases discussed in Section 4.2, exhibited Z_{DR} biases of 0.66 dB and 0.68 dB, respectively. Finally, once all corrections are completed, the radar data are smoothed along each ray using a cubic spline approach.

2.2 Complementary data

In addition to the polarimetric radar data, both field campaigns offer additional datasets for contextualizing our results. The PICASSO field campaign offers about 24 hours of in-situ aircraft observations, which are used to evaluate our retrievals and better understand the variability of cloud ice properties on fine spatial scales. Likewise, ground-based aerosol

observations from BAECC are used in concert with activated ice nucleating particle (INP) parameterizations to estimate the expected cloud ice *N* and identify potential SIP events.

2.2.1 In-situ aircraft observations from PICASSO

During PICASSO, FAAM performed multiple transects from Chilbolton to Exeter, UK (~150 km) and back at varied altitudes above, and within, the melting layer (ML). Figure 2.1 depicts the flight path for the 13 February 2018 flight, which was typical of other flights during the campaign.

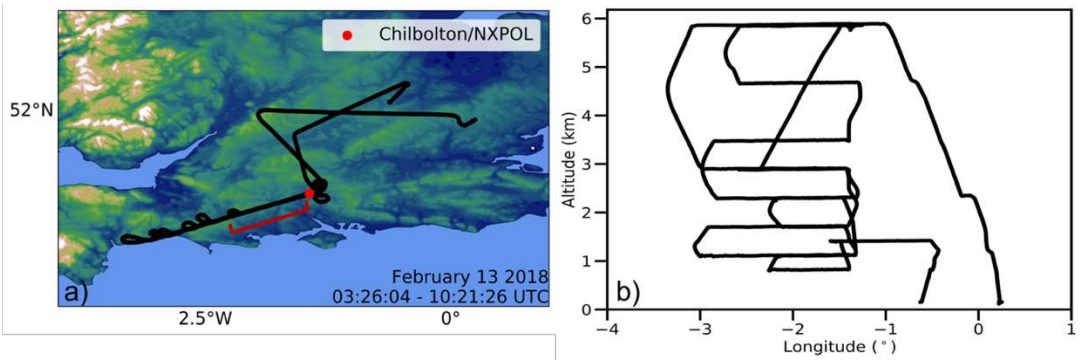

Figure 2.1. (a) Flight path and (b) altitude (km) on 13 February 2018 between 3:00 UTC and 10:30 UTC. The red dot in a) denotes the location of Chilbolton, UK and NXPol and the red bracket denotes the approximate path over which retrievals are evaluated in Section 4.1.

Flight-level atmospheric temperature was measured using a deiced Rosemount sensor (Taylor et al. 2015), while liquid water content (LWC) and total water content (TWC) were measured using a Nevzorov probe (Korolev et al. 1998). The PSD was measured with multiple optical array probes, including a Stratton Park Engineering Company Two-Dimension Stereo (2DS) probe and High-Volume Precipitation Spectrometer (HVPS). The 2DS measures particles between 5–1285 μm with a resolution of 10 μm. The HVPS measures larger particles between 75–19275 μm with a resolution of 150 μm. All aforementioned in-situ datasets are recorded at 1 s resolution, but are averaged to 5 s intervals to enhance statistical reliability (Protat et al. 2007)

while ensuring a sufficient number of samples (≥30 for this study) for comparison against retrievals. We focus our analysis on the HVPS observations because the instrument is able to capture a much larger range of particle sizes than the 2DS, including those that dominate the radar signal. The PSDs are truncated below 300 μm, as HVPS observations below this threshold are considered unreliable due its 150 μm resolution (Glienke and Mei 2020) and are known to be influenced by shattered particles with diameters < 500 μm (Korolev et al. 2011). We recognize that the lower HVPS bound of 300 μm is insufficient to characterize SIP events and the onset of primary ice nucleation, both of which are characterized by much smaller pristine ice crystals. As previously stated, our purpose here is to first evaluate the efficacy of our retrieval framework, then use the BAECC data to study SIP events and other microphysical processes. Furthermore, as discussed in Section 4.1, our evaluation focuses on cases with strong polarimetric signal, which are likely associated with advanced stages of ice growth (i.e. larger pristine ice crystals and active aggregation). Nonetheless, it will be valuable to combine 2DS and HVPS PSDs in future evaluation efforts.

Three metrics are chosen to evaluate our retrievals: N (denoted as N_{FAAM}), q_I (denoted as $q_{I,FAAM}$), and PSD shape. N_{FAAM} is obtained by integrating the PSD and has an instrument uncertainty that is a function of airspeed and sample volume (Gleinke and Mie 2020). For a nominal airspeed of 100 m s^{-1}, the HVPS sample volume is 310 L s^{-1}. If N_{FAAM} is 0.5 L^{-1} sampled at 1 s resolution, then the uncertainty goes as $\frac{\sqrt{0.5 \cdot 310 \cdot 1}}{310} = 0.04$ L^{-1} via Poisson counting statistics (Gleinke and Mie 2020).

$q_{I,FAAM}$ is calculated by two methods. First, $q_{I,FAAM}$ is derived from the difference between the TWC (denoted as $q_{T,FAAM}$) and LWC (denoted as $q_{L,FAAM}$) measured by the Nevzorov probe. Both $q_{T,FAAM}$ and $q_{L,FAAM}$ were corrected for changes in aircraft altitude and

environmental conditions, as in Abel et al. (2014). However, from wind tunnel tests, Korolev et al. (2013a) demonstrated that Nevzorov-derived $q_{I,FAAM}$ is systematically underestimated when environmental q_I exceeds several g m^{-3}, due to pooling water in the TWC probe. Hence, we include a second method, deriving q_I from HVPS PSDs using a set of mass-size relationships listed in Mason et al. (2018). These relationships, derived from aircraft in-situ and surface observations, are formulated as:

$$m = aD^b \tag{2.1}$$

where m is the mass of the particle, D is the particle diameter, and a and b are the pre-factor and exponent, respectively (see Table 2.2 for coefficients, Figure 2.2 for their variability). q_I is then given as:

$$q_I = \int_0^\infty aD^b n(D) dD \tag{2.2}$$

where n is the number concentration at a given particle diameter D.

Finally, the shape of observed and retrieved PSDs are compared. Retrieved pristine ice and snow aggregate PSDs are merged to the HVPS size bins and compared against HVPS PSDs using root mean squared error (RMSE) as a metric for agreement. As FAAM observed both ice and liquid phases during its flights, we define in-cloud samples as having $q_{T,FAAM} > 0.01$ g m^{-3}. Only in-cloud samples will be considered for intercomparison.

In addition to these three metrics, it would be ideal to evaluate the partitioning between pristine ice and snow aggregates in our retrieval. However, separating two species in in-situ data is nontrivial and, while such algorithms exist, is beyond the scope of this work. Nevertheless, these three metrics together enable a holistic assessment of our retrieval and its physical validity. For example, incorrect partitioning between pristine ice crystals and snow aggregates in our retrieval will manifest as errors in q_I and PSD shape, even if N is retrieved correctly. Such an

approach is therefore critical for identifying and diagnosing any biases that may exist in our retrieval framework.

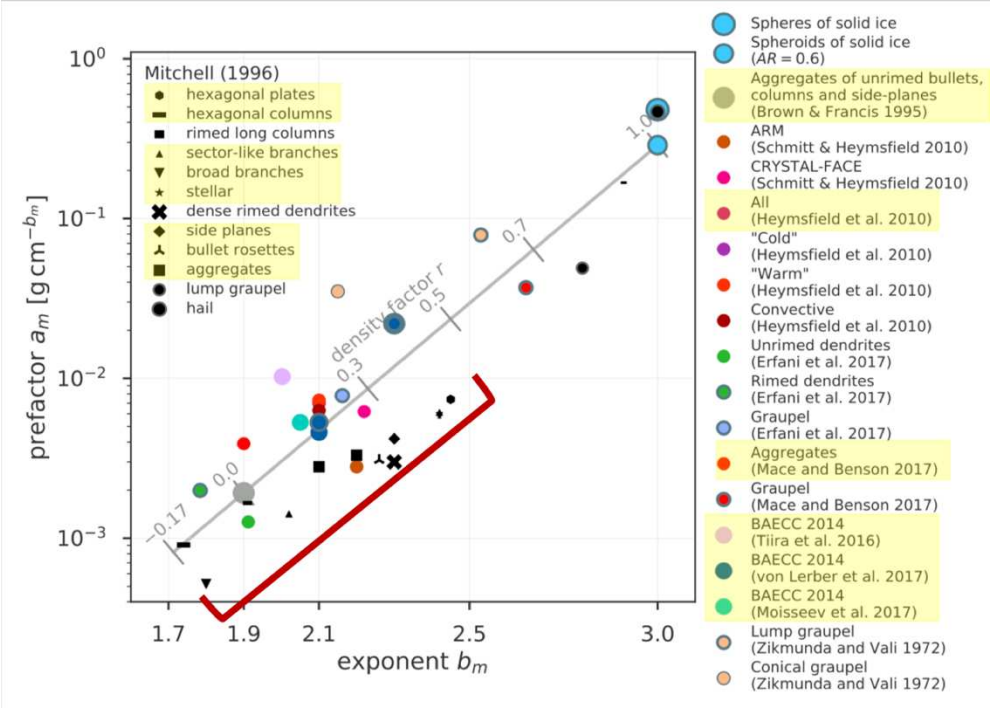

Figure 2.2. A plot of pre-factors (a) and exponents (b) in mass-size relationships for various pristine ice and aggregate habits, adapted from Mason et al. (2018). The red bracket shows the approximate range of values of a and b used for calculating q_I in equation (2.2), which correspond to relationships highlighted in yellow and listed in Table 2.2. Note that the density factor (r) shown in the figure is not used in the study; r was designed to represent the mass-size relationship in a continuum manner between unrimed and rimed particles.

Table 2.2. Mass-size relationships (a subset of Figure 2.2; denoted by yellow shading) used to calculate ice water content from in-situ particle size distributions. Note that the relationships of stellar and broad branches (in bold) were respectively used to build low density (LD) and high density (HD) aggregates in the scattering table (see Section 3.2.1).

Habit	a (g cm^{-b})	b	Reference
Stellar	**0.00027**	**1.67**	Mitchell (1996)
Hexagonal columns	0.000907	1.74	
Broad branches	**0.000516**	**1.80**	
Sector-like branches	0.00142	2.02	
Bullet rosettes	0.00308	2.26	
Side planes	0.00419	2.3	
Hexagonal plates	0.00739	2.45	
Aggregates	0.0028	2.1	
Aggregates	0.0039	1.9	Mace and Benson (2017)
Aggregates of unrimed bullets, columns, and side-planes	0.00185	1.9	Brown and Francis (1995)
Unrimed dendrites	0.001263	1.912	Erfani and Mitchell (2017)
Not specified	0.007	2.2	Heymsfield et al. (2010)
Not specified	0.01036	2.002	Tiira et al. (2016)
Not specified	0.0053	2.05	Moisseev et al. (2017)
Not specified	0.0046	2.1	von Lerber et al. (2017)

2.2.2 Ground-based aerosol and INP observations at Hyytiälä

While in-situ measurements provide a direct comparison for evaluations, we also perform indirect comparisons, investigating how retrieved pristine ice N compares against the expected

primary ice N. This approach is also useful for identifying potential regions of secondary ice production (SIP), a moniker for processes by which pristine ice forms via mechanisms other than traditional homogenous/heterogenous freezing and rapidly yields orders of magnitude enhancement in N.

Primary ice N is estimated using two parameterizations of activated INPs. The first parameterization, described in DeMott et al. (2010), is given as:

$$N_{INP,D}^{*} = a(273.16 - T)^{b}(N_{aer>0.5\,\mu m})^{c(273.16-T)+d}, \tag{2.3}$$

which requires knowledge of the atmospheric temperature (T) and the number concentration of aerosol particles with diameters exceeding 0.5 μm ($N_{aer>0.5\,\mu m}$) at standard temperature and pressure (STP). This parameterization was based on INP and aerosol observations from aircraft and ground-based observational studies and is intended to describe a global average INP distribution. As such, its generalizability makes it a sound choice for providing a first order estimation of expected primary ice N. During BAECC, hourly-averaged aerosol size distributions over the range of 0.5–20 μm were available from a ground-based aerodynamic particle sizer operated by the University of Helsinki since 1996. To be used in equation (2.3), the measured size bins were converted from aerodynamic diameter to geometric diameter following Virkkula et al. (2011). Once the predicted number concentration (N_{INP}^{*}) at STP is derived, it needs to be converted to ambient atmospheric conditions, using

$$N_{INP} = N_{INP}^{*}\left(\frac{T}{P}\right)_{\mathrm{STP}}\left(\frac{P}{T}\right), \tag{2.4}$$

where $N_{INP,D}$ is the final predicted primary ice N and P is the ambient atmospheric pressure. Values for coefficients *a–d* used in equation (2.3) can be found in Table 2.3

The second parameterization, proposed by Schneider et al. (2020), was based on year-long filter-based INP collections (and post-processing via an immersion freezing method) at

Hyytiälä in 2019, making it ideal for evaluating our retrieval. Instead of using aerosol number concentration, Schneider et al. (2020) incorporated surface temperature (T_{sfc}) in their parameterization as a proxy for the seasonal variability of INP concentration in the Hyytiälä boreal forest environment, given as:

$$N^*_{INP,S} = 0.1\exp\left(aT_{sfc} + b\right)\exp(cT + d) \tag{2.5}$$

where T is the INP activation temperature (strictly valid for 250 to 265 K). In our calculations, we use the atmospheric temperature as the INP activation temperature. $N^*_{INP,S}$ must also be converted from STP to ambient conditions using equation (2.4). Similarly, the coefficient *a–d* can be found in Table 2.3.

Table 2.3. Coefficients used in equations (2.3) and (2.5) for ice nucleating particle parametrizations described in DeMott et al. (2010) and Schneider et al. (2020).

	Coefficient			
	a	b	c	d
DeMott et al. (2010)	0.0000594	3.33	0.0264	0.0033
Schneider et al. (2020)	0.074 ± 0.006	–18 ± 2	–0.504 ± 0.005	127 ± 1

2.2.3 Bulk properties from empirical relationships

In addition to comparison with INP concentration, we also use bulk N, q_I, and D_0 derived from empirical relationships described in Ryzhkov et al. (2018) and Murphy et al. (2020). These relationships are based on similar radar observables (i.e., Z_{H}, Z_{DR}, K_{DP}) with the additional radar observable Z_{DP} ($Z_{\mathrm{DP}} = Z_{\mathrm{h}} - Z_{\mathrm{v}}$; mm^{-6} m^{-3}). The relationships are given as:

$$\log N = 0.1Z_{\mathrm{H}} - 2\log\frac{Z_{\mathrm{DP}}}{K_{\mathrm{DP}}\lambda} - 1.11 \tag{2.6}$$

$$q_I \approx 0.004 \left(\frac{K_{\mathrm{DP}}\lambda}{1-Z_{\mathrm{dr}}{}^{-1}}\right) \tag{2.7}$$

$$D_0 = -0.1 + 2\left(\frac{Z_{\mathrm{DP}}}{K_{\mathrm{DP}}\lambda}\right)^{\frac{1}{2}} \tag{2.8}$$

where Z_{H} is in units of dBZ, K_{DP} is in units of ° km^{-1}, Z_{dr} is unitless ($Z_{\mathrm{dr}} = 10^{0.1Z_{\mathrm{DR}}}$), and λ is the radar wavelength in mm. N, q_I, and D_0 are given in units of L^{-1}, g m^{-3}, and mm, respectively. Such relationships do not consider the individual contributions from different species, but rather report a combined, or bulk, value.

Murphy et al. (2020) evaluated this parameterization against collocated in-situ observations in the trailing stratiform region of a mesoscale convective system over Oklahoma (Figure 2.3). Limited error statistics were provided in Murphy et al. (2020), but Figure 2.3 shows that their estimated D_0 and q_I tend to be systematically biased low and N scatters significantly with respect to in-situ measurements. Figure 2.3 also shows that the performance of other estimates largely depends on the cloud systems that were used to derive the empirical relationships. For example, the Z_{H}-D_0 relationships described in Matrosov et al. (2019) and Skofronick-Jackson et al. (2019) represent heavy snow cases, explaining the larger estimated D_0. The Z_{H}-q_I relationship in Hogan et al. (2006) was based on cirrus clouds, explaining the lower estimated q_I. This highlights the need for a method that can distinguish contributions between pristine ice and snow aggregates for ice- and mixed-phase clouds, to avoid any intrinsic retrieval limitations.

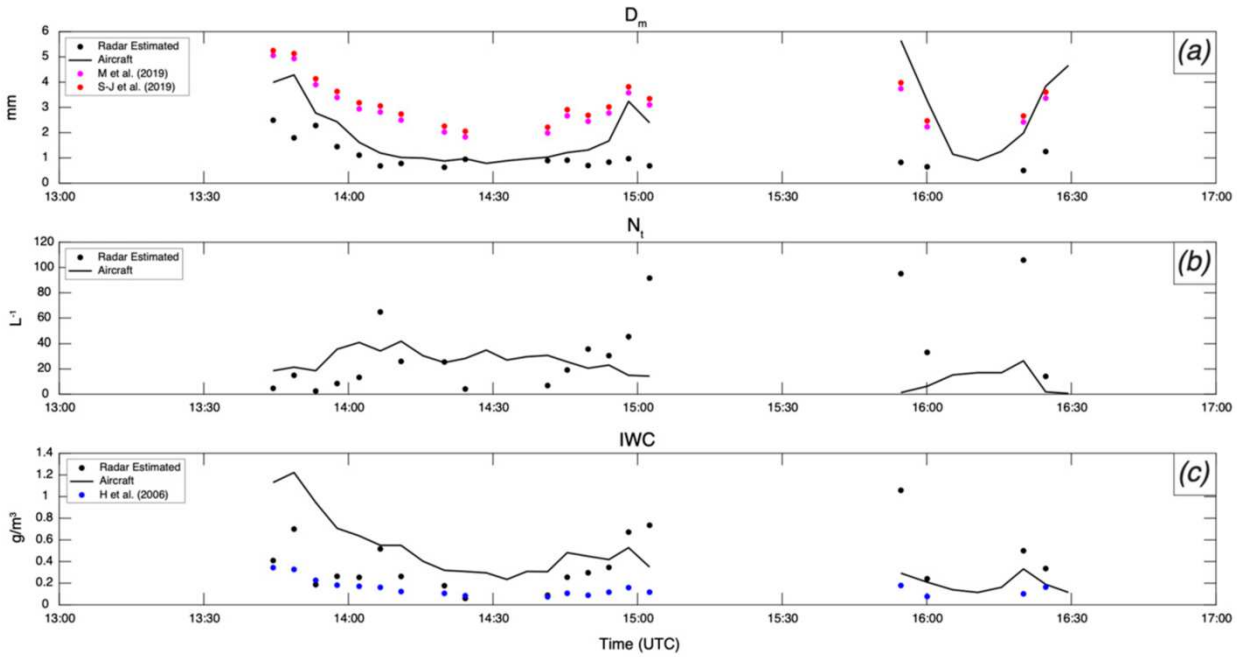

Figure 2.3. Comparisons between in-situ measurements (solid lines) and ice microphysical properties of a) D_0, b) N, and c) q_I estimated from a number of empirical relationships. This figure is taken from Murphy et al. (2020). Properties estimated from Murphy et al. (2020), Matrosov et al. (2019), Skofronick-Jackson et al. (2019), and Hogan et al. (2006) are denoted by black, magenta, red and blue dots, respectively.

CHAPTER 3

Methodology

This section introduces the method by which polarimetric radar data is used to retrieve N, D_0, and q_I of pristine ice and snow aggregates for each radar gate. Details for practical implementations are given in Section 3.3.2.

3.1 Particle size distribution (PSD)

We approximate the PSD of pristine ice and aggregates by normalized Gamma distributions, given as (Testud et al., 2001):

$$n(D_M) = N_0 f_\mu \left(\frac{D_M}{D_0}\right) \tag{3.1}$$

where n is the number concentration at a given particle maximum dimension (D_M), N_0 is the normalized number concentration, and D_0 is the median volume diameter. Equation (3.1) uses D_M, because the particles in the scattering database required for modeling radar observables are described by their discrete maximum dimensions. The function f_μ is defined as:

$$f_\mu \left(\frac{D_M}{D_0}\right) = \frac{6}{3.67^4} \cdot \frac{(3.67+\mu)^{4+\mu}}{\Gamma(4+\mu)} \cdot \left(\frac{D_M}{D_0}\right)^\mu \cdot \exp\left[-(3.67+\mu)\frac{D_M}{D_0}\right] \tag{3.2}$$

where μ is the shape parameter of the PSD; $\mu = 0$ corresponds to an exponential distribution. Following Mason et al. (2018) and Fielding et al. (2015), we assume a constant shape parameter of $\mu = 2$. The retrieval uncertainty introduced by varying μ will be discussed in 3.3.2, although a number of studies have shown that the retrieved ice water content is relatively insensitive to the choice of shape parameter (Delanoe et al. 2005; Spek and Unal. 2007).

From the PSD, N and q_I can be respectively computed by:

$$N = \int_0^\infty n(D_M) dD_M = N_P + N_A \tag{3.3}$$

$$q_I = \int_0^\infty m(D_M) n(D_M) dD_M = q_{I,P} + q_{I,A} \tag{3.4}$$

where m is the mass of the particle and the subscripts P and A denote contributions from pristine ice and snow aggregates, respectively. In practice, the relationship between particle mass and maximum dimension, and the integration limits in equations (3.3) and (3.4) are dictated by the scattering database used in the retrieval process, which is discussed next.

3.2 Simulating radar observables

3.2.1 Single scattering properties of ice

To model polarimetric radar observables from the PSD, knowledge of the single scattering properties of ice particles is required. While many scattering databases of realistically shaped ice particles at millimeter wavelengths are available, we use Lu et al. (2016) for the following reasons. Many existing scattering databases assume total random orientation of the scatterers (e.g., Liu (2008), Hong et al. (2009), Kuo (2016) and Eriksson et al. (2018)). Such assumption cannot explain polarimetric radar signals which are produced by non-spherical scatterers exhibiting preferred orientations with respect to the zenith direction. The database of Brath et al. (2020) assumes scatterers possess arbitrary fixed orientations relative to the zenith direction, but only includes hexagonal plates and aggregates consisting of hexagonal plates. We found that the database described in Lu et al. (2016) fits our needs in the current polarimetric radar study, since it contains all necessary polarimetric scattering data in a large number of fixed orientations for a wide variety of ice crystal species commonly observed in mixed-phase temperature regimes. Information on species relevant to this study is given in Table 3.1, including plates, columns, dendrites, and aggregates. The single scattering properties for each

species are available for a range of crystal maximum dimensions, thickness ratios, and types. The maximum dimensions of pristine habits generally begin at ~0.1 mm and do not exceed 6 mm, whereas the aggregates begin at ~0.4 mm and extend to 18 – 45 mm. This variability in the upper bound of aggregate maximum dimension is a function of the monomers used to construct the aggregates. Aggregates comprised of either stellar crystals or needles, both with low density and high-density configurations, are available in the database. Multiple morphological realizations per maximum dimension are available for dendrites and aggregates to account for their complexities.

The scattering calculations were conducted using the generalized multi-particle Mie method (GMM; Xu, 1995) and the discrete dipole approximation (Yurkin and Hoekstra, 2011). We used properties calculated from GMM, because the latter is not available for aggregates. Specifically, we use the amplitude scattering matrix elements in the forward and backward direction for horizontally and vertically polarized radiation, denoted as $S_{hh}^{f,b}$ and $S_{vv}^{f,b}$ where the superscript and subscript respectively represent the scattering direction and the polarization status. These elements are tabulated for various azimuth and elevation angles. As the azimuthal orientation of hydrometeors relative to the radar is random and unknown, these elements are azimuthally averaged for each ice crystal prior to computing the radar moments. $S_{hh}^{f,b}$ and $S_{vv}^{f,b}$ are also linearly interpolated with respect to elevation angles for radar rays. The properties of dendrites and aggregates with multiple habit realizations per discrete maximum dimension are also averaged, because the exact morphological characteristics of these particles at any given time in nature are also unknown.

Table 3.1. Characteristics of particles included in the scattering database presented in Lu et al. (2016). The maximum dimensions of the particles in the database are equally spaced in logarithmic space. The dimensional relationships used to create each particle are given in Pruppacher and Klett (1997). The mass-size relationship used to define the density of aggregates in the database is given in Mitchell et al. (1996). For plates and dendrites, h and D are the thickness and maximum dimension (mm) of the particle, respectively. For columns, d and L are the maximum dimension (mm) of the basal face and column length, respectively.

Habit*	**Size range (mm)**	**Type/thickness ratio*#**	**Dimensional relationship**	**Mass-size relationship**
Aggregates	0.37 – 41.32	LD-N1e	$d = 0.03527L^{0.437}$	LD: $0.000270D^{1.67}$ HD: $0.000516D^{1.80}$
	0.60 – 16.84	HD-N1e		
	0.43 – 62.91	LD-P1d	$h = 0.00996D^{0.415}$	
	0.41 – 42.51	LDt-P1d		
	0.41 – 40.56	HD-P1d		
Dendrites (P1e)	0.50 – 5.63	0.5	$h = 0.009022D^{0.377}$	—
	0.50 – 5.63	1.0		
Plates (P1a)	0.10 – 2.01	0.5	$h = 0.0141D^{0.474}$	
	0.10 – 2.54	1.0		
	0.11 – 2.51	2.0		
Columns (N1a)	0.18 – 4.17	1.0	$d = 0.030487L^{0.61078}$	
	0.19 – 4.31	2.0		

Abbreviations denote the type of pristine ice crystal and are defined in Pruppacher and Klett (1997;* Figure 2–38). LD and HD refer to low- and high- density aggregate configurations, respectively. #Thickness ratios are used to expand the range of dimensional relationships used to construct the pristine crystals.

3.2.2 Radar equations

From the assumed PSD and the amplitude scattering matrix elements mentioned above, we compute radar observables for a single sample volume containing multiple ice particle habits, given as:

$$Z_h = \frac{4\lambda^4}{\pi^4|K_w|^2}\sum_{i=1}^{J}\int_0^{\infty}\left\{A\left|S_{hh,i}^{b}\right|^2 + B\left|S_{vv,i}^{b}\right|^2 + 2CRe\left[S_{hh,i}^{b}S_{vv,i}^{b\,*}\right]\right\}n(D_M)dD_M \quad (3.5)$$

$$Z_v = \frac{4\lambda^4}{\pi^4|K_w|^2}\sum_{i=1}^{J}\int_0^{\infty}\left\{B\left|S_{hh,i}^{b}\right|^2 + A\left|S_{vv,i}^{b}\right|^2 + 2CRe\left[S_{hh,i}^{b}S_{vv,i}^{b\,*}\right]\right\}n(D_M)dD_M \quad (3.6)$$

$$Z_{hv} = \frac{4\lambda^4}{\pi^4|K_w|^2}\sum_{i=1}^{J}\int_0^{\infty}\left\{C\left[\left|S_{hh,i}^{b}\right|^2 + \left|S_{vv,i}^{b}\right|^2\right] + A\left[S_{hh,i}^{b}S_{vv,i}^{b\,*}\right] + B\left[S_{vv,i}^{b}S_{hh,i}^{b\,*}\right]\right\}n(D_M)dD_M \quad (3.7)$$

$$Z_{dr} = \frac{Z_h}{Z_v} \quad (3.8)$$

$$\rho_{hv} = \frac{|Z_{hv}|}{[(Z_h)(Z_v)]^{1/2}} \quad (3.9)$$

$$K_{DP} = \frac{0.18\lambda}{\pi}\sum_{i=1}^{J}\int_0^{\infty}\left\{C_k\mathrm{Re}\left[S_{hh,i}^{f} - S_{vv,i}^{f}\right]\right\}n(D_M)dD_M \quad (3.10)$$

where λ is the radar wavelength. K_w is the dielectric factor of water and $|K_w|^2 = 0.93$. The vertical bars represent the magnitude of the terms within, while Re represents the real part of the complex number and the asterisk indicates its complex conjugate. The index *i* represents the species existing in the radar volume, and the index *J* represents the number of species. Coefficients *A*, *B*, *C*, and C_k are included to account for the effects of canting on the polarimetric radar moments. Following Jung et al. (2010) and Ryzhkov et al. (2011), the canting angle distributions are assumed to be Gaussian, and their effects can be parameterized using the mean and standard deviation of the distribution. Supposing that all oblate species fall with their major axes preferentially oriented in the horizontal plane, the mean canting angle can be set to zero (Ryzhkov et al. 2011). The width of the canting angle distribution is set to 10° for pristine ice

crystals and 40° for snow aggregates, similar to Ryzhkov et al. (2011) and Matsui et al. (2019). All detailed equations and coefficients can be found in Jung et al. (2010).

3.3 The retrieval method

3.3.1 The basis

To combine various radar observables and properly account for their uncertainty, we use ENCORE-ICE to provide ray-by-ray estimates of ice particle properties. ENCORE has previously been used to retrieve three-dimensional cloud microphysical properties (Fielding et al. 2014) and one-dimensional cloud and drizzle properties (Fielding et al. 2015). We use the same framework but have modified a number of key components for ice cloud retrieval (ENCORE-ICE).

The state vector (i.e., variables to be retrieved) for each ensemble member is defined as:

$$\boldsymbol{x} = \left(\log N_{0,P}^{(i=1\ldots m)}, \log D_{0,P}^{(i=1\ldots m)}, \log N_{0,A}^{(i=1\ldots m)}, \log D_{0,A}^{(i=1\ldots m)}\right) \tag{3.11}$$

where the superscript i represents the index of the range gate along a ray and, again, subscripts P and A denote pristine ice and aggregates, respectively. The total number of gates to be retrieved in said ray is m. Let us use Q members to form an ensemble, i.e.,

$$\boldsymbol{X} = \left(\boldsymbol{x}_1, \ldots, \boldsymbol{x}_Q\right) \tag{3.12}$$

such that the mean of $\boldsymbol{X}$ represents the best estimate of the state vector, and the spread of the ensemble members around the mean represents the uncertainty in the best estimate.

To find the best estimate of the state vector given the observations, each ensemble member is updated iteratively using the iterative Kalman Filter equations (Evensen 1994; Gu and Oliver 2007), given as:

$$\boldsymbol{x}_k^{j+1} = \boldsymbol{x}_k^j + \boldsymbol{K}^j\left(\boldsymbol{y}_k^j - h\left(\boldsymbol{x}_k^j\right) - \varepsilon_k\right) - \left(1 - \boldsymbol{K}^j\boldsymbol{H}^j\right)\left(\boldsymbol{x}_k^j - \boldsymbol{x}_k^0\right) \tag{3.13}$$

where the superscripts j and $j+1$ indicate the current and updated iteration, respectively. The subscript k is the index of the ensemble member. $\boldsymbol{x}_k^0$ represents the prior (initial) or background state of the ensemble member k. The observation vector $\boldsymbol{y}$ is defined by gate-by-gate radar observables introduced in the previous section:

$$\boldsymbol{y} = \left(Z_{\mathrm{H}}^{(i=1\ldots m)}, Z_{\mathrm{DR}}^{(i=1\ldots m)}, L^{(i=1\ldots m)}, K_{\mathrm{DP}}^{(i=1\ldots m)}\right) \tag{3.14}$$

where

$$L = -\log(1-\rho_{\mathrm{HV}}) \tag{3.15}$$

as introduced by Keat et al. (2016) due to its preferential Gaussian nature. Z_{H} and Z_{DR} are in their logarithmic form in equation (3.14). $h(\boldsymbol{x})$ represents the forward model with $\boldsymbol{H}$ as its linearization. **K** is the Kalman gain and controls how much weight is placed on the observations compared to the current state. Both **K** and **H** can be calculated using the ensemble members, through:

$$\mathbf{E}_x = \left[\boldsymbol{x}_1 - \overline{\mathbf{X}}, \ldots, \ \boldsymbol{x}_Q - \overline{\mathbf{X}}\right] \tag{3.16}$$

$$\mathbf{E}_y = \left[h(\boldsymbol{x}_1) - \overline{h(\mathbf{X})}, \ldots, \ h\left(\boldsymbol{x}_Q\right) - \overline{h(\mathbf{X})}\right] \tag{3.17}$$

where the bar represents the mean. Detailed equations can be found in Fielding et al. (2014) and Chiu et al. (2020). Observational uncertainty, ε_k , is accounted for in each iteration by perturbing $h(\boldsymbol{x})$ randomly using a Gaussian distribution with zero mean and standard deviations given in Table 3.2.

3.3.2 Practical considerations

There are a number of practical considerations for ENCORE-ICE implementation. The first is the consideration of ice habits. While the scattering database provides three habits for pristine ice (see Table 3.1), we choose plates as our prescribed habit. This choice is partly based on the temperature range found in our cases from the PICASSO and BAECC campaigns. As

shown in Figure 3.1, the mean temperature is –11.4 ± 6.4°C. 39% of gates for retrieval are in the range between –10°C and –20°C, in which plates and dendrites are the most likely habit present, whereas 30% of gates are between –10°C and –5°C, in which columns are the most likely habit (Magono 1962; Pruppacher and Klett 1997, pp. 44). Since there are slightly more gates between –10°C and –20°C, plates and dendrites can be a good prescribed choice for our retrieval. Plates typically have larger backscattering cross sections, and thus Z_{H}, than dendrites (Figure 3.2). If both species are present in similar concentrations, plates will dominate the radar signal. Furthermore, when plates and dendrites are possibly of similar size early in their lifespan, their backscattering cross sections are similar and their radar signals become indistinguishable from one another, yielding little impact on retrieval solution. These findings, which are consistent with Spek and Unal (2007), suggest that the habit of plates would be more robust compared to dendrites. However, considering that the number of gates for retrieval in the range between –10°C and –5°C is not negligible, the uncertainty in habit still needs to be accounted for. Moving forward, each retrieval will be rerun with columns and dendrites; the difference in the retrieved means compared to the runs with plates will be used to quantify the retrieval uncertainty due to habit choice.

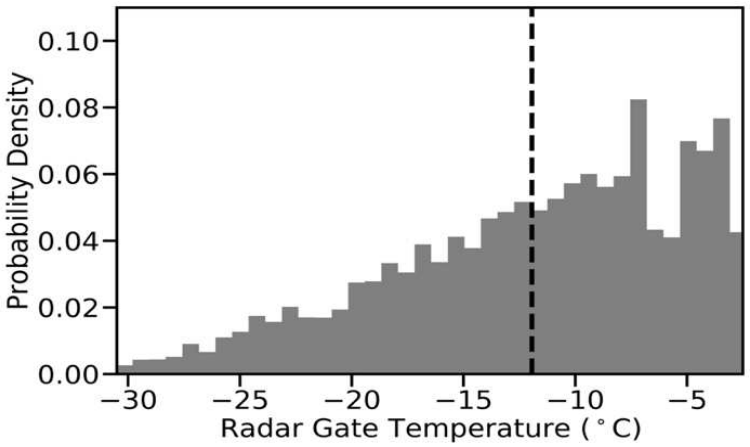

Figure 3.1. Probability density distribution of atmospheric temperature (°C) for all radar gates considered in this study, obtained from collocated atmospheric soundings. The vertical dashed black line denotes the mean of the distribution.

Table 3.2. Estimated observational errors for X-band observables. Adapted from Bringi and Chandrasekar (2005; 359–375) and Wang and Chandrasekar (2009).

Observable	**Uncertainty**
X-band horizontal reflectivity (Z_{H})	0.5 dBZ
X-band differential reflectivity (Z_{DR})	0.05 dB
X-band specific differential phase shift (K_{DP})	0.1° km^{-1}
Co-polar correlation coefficient (ρ_{HV}) recast as L; equation (3.15)	0.1* (unitless)

*Uncertainty is a function of ρ_{HV} itself. 0.1 is quoted based on $\rho_{\mathrm{HV}} = 0.95$

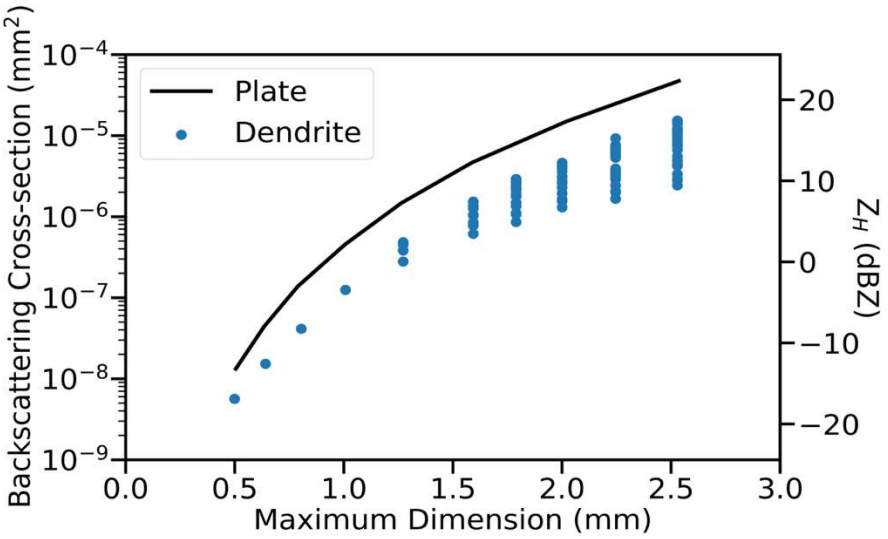

Figure 3.2. Backscattering cross-section (mm^2) and Z_H (dBZ) of plates and dendrites (1.0x thickness ratio) at side incidence (0°) for varying particle maximum dimensions given in the scattering database, with a nominal N = 1 L^{-1}. The spread about a given dendrite maximum dimension is the result of different dendrite morphologies.

Similarly, the scattering database provides five types of aggregates; two of them were constructed using ice columns (LD-N1e and HD-N1e), two of them using stellar ice crystals (LD-P1d and LDt-P1d) and the other one using broad branches (HD-P1d). The aspect ratios of aggregates in nature are known to vary depending on the pristine habits that comprise them. Defining an aspect ratio as the ratio of the lengths of the minor axes to the major axes, Garrett et al. (2015) and Jiang et al. (2017) observed aspect ratios ranging from 0.3 to 0.6 for falling aggregates at the surface. As shown in Figure 3.3, among the aggregates available in the scattering database, LDt-P1d and HD-P1d exhibit aspect ratios within the observed range. Since HD-P1d was built using a mass-size relationship closer to other types of aggregates in Figure 2.2 and Table 2.2, we select HD-P1d as the prescribed choice for retrieval.

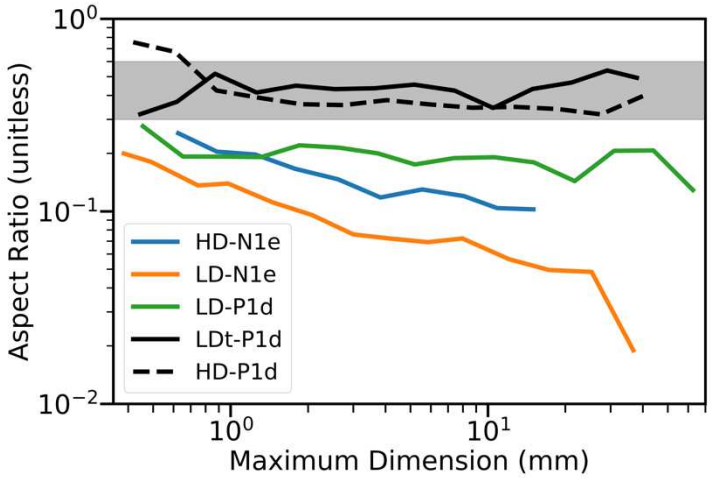

Figure 3.3. Aspect ratios of various aggregate types available in the scattering database as a function of their maximum dimensions. Aspect ratio is defined as the ratio of the lengths of the minor axes to the major axes. The grey shading between 0.3 and 0.6 represents the typical range of snow aggregate aspect ratios observed in nature (Garrett et al. 2015; Jiang et al. 2017).

Table 3.3. The prior and uncertainty used in ENCORE-ICE.

Variable	Mean Value	Standard deviation
Pristine Ice		
N_0 (L^{-1} mm^{-1})	100	±16%
D_0 (mm)	0.5	±16%
Aggregate		
N_0 (L^{-1} mm^{-1})	1	±16%
D_0 (mm)	1.25	±16%

The second consideration is the prior used to generate the first guess for ensemble members. Using over 70 hours of in-situ aircraft observations from a wide range of field campaigns spanning diverse cloud and temperature regimes, Delanoe et al. (2014) characterized the PSDs of ice particles by normalized Gamma distributions (i.e., equation (3.1)), and found

that N_0 ranged between 1 L^{-1} mm^{-1} and 10,000 L^{-1} mm^{-1} with a mean 100 L^{-1} mm^{-1}, and D_0 ranged between 0.2–0.8 mm with a mean of 0.5 mm for the temperature zone of –10°C to –20°C. We therefore choose their means for the prior of the pristine ice. Similarly, Tiira et al. (2016) analyzed surface measurements of ice particle PSDs from the Precipitation Imaging Package (PIP; Newman et al., 2009) during BAECC. They found that N_0 ranged from 1 L^{-1} mm^{-1} to 1000 L^{-1} mm^{-1} and D_0 ranged from 0.5 mm to 4 mm. As these were surface based, the measured PSDs are more representative of the characteristics of snow aggregates. Hence, we use N_0= 1 L^{-1} mm^{-1} and D_0 = 1.25 mm as the prior of aggregates. Since the ranges in these is seen to be quite wide, the uncertainty in our prior should be accordingly assigned to be large. For a sufficiently wide-spread prior, the information of the prior will get lost effectively during iterations, and the solutions will better agree with observations. In its current state, our state vector varies by approximately ±20% (as shown in Table 3.3). We recognize that this spread is likely not sufficient and retrieval performance associated with a wider initial state vector is currently under investigation.

The third consideration is the assumption in shape parameter μ used to formulate PSDs in equation (3.1). Tiira et al. (2016) derived μ values for hydrometeor PSDs observed at the surface associated with 23 separate snow events during BAECC; they found that μ values ranged from –2 to 6, with a distribution roughly centered at $\mu = 0$ (i.e. exponential). The average percent error in retrieved N and q_I for the aforementioned range of μ observed during BAECC is given in Figure 3.4, with respect to the retrieval using $\mu = 2$. Percent error in N is considerable for $\mu < 0$, but within 50% for $\mu \geq 0$. Percent error in q_I is much more modest, never exceeding 20% and typically within 10%. This supports Delanoe et al. (2005) and Spek and Unal (2007), who found that the choice of μ contributes the least to uncertainty in retrieved q_I.

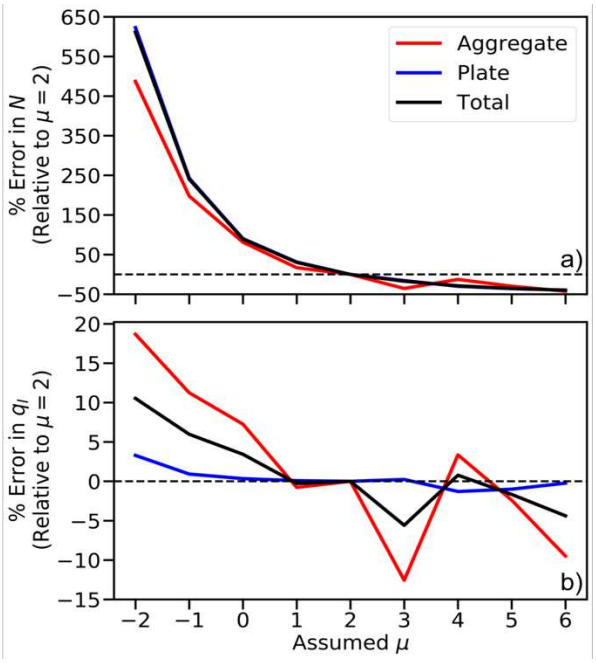

Figure 3.4. Percent error in retrieved N (a) and q_I (b) for various assumed μ values, with respect to retrieval using μ = 2. Blue lines denote pristine ice, red lines denote snow aggregates, and black lines the total (not their respective sums). Horizontal dashed black lines denote the 0% error line.

The fourth consideration is the number of the ensemble members required in ENCORE-ICE. The number of the ensemble members must be sufficient to suppress spurious correlations in the state vector. Here, we define sufficient as greater than or equal to the size of the state for the ensemble retrieval method. For a nominal cloud layer of 3 km with a sample resolution of 30 m, this corresponds to 100 gates along a ray and thus a size of 100 (number of gates) x 4 (number of state variables) of the state vector. This then requires at least 400 ensemble members for each ray. In our retrieval, we use 500 ensemble members for each ray to meet this requirement and account for rays that contain more than 100 retrievable gates. Additionally, we stop the iteration process after the 10th iteration, because the value of the cost function does not change significantly afterwards.

Finally, to ensure that gates are associated with good quality and sufficient information for our method, we exclude gates that exhibit one or more of the following:

- Gates within 500 m of the 0°C level, to avoid contamination from liquid or multi-phase (i.e. melting) hydrometeors in the radar sample volume because our state vector is not designed for that.
- Gates where ρ_{HV} exceeds 1.0, because these values are unphysical.
- Gates with a signal-to-noise ratio (SNR) less than 25 dB, because of a lack of detectable hydrometeors. This threshold was chosen because the precipitating region and its surrounding area typically have SNR values in excess of 30–40 dB.
- Radar rays with elevation angles greater than 50°, because Z_{DR} tends towards 0 dB at higher elevation angles and polarimetric information becomes ambiguous.
- Gates with Z_{DR} below 0.25 dB, regardless of their elevation angles, because the relative contributions of pristine ice and aggregates become ambiguous at lower values, as indicated in Keat and Westbrook (2015; Figure 3).
- Gates with negative K_{DP}, indicative of conical graupel (Aydin and Seliga 1984) or the vertical reorientation of pristine ice crystals in the presence of thunderstorm electric fields (Hubbert et al. 2014). Since the state vector only includes pristine ice and aggregates, we exclude such gates as well.

CHAPTER 4

Results

4.1 Retrieval evaluation using PICASSO data

The case of 13 February 2018 from the PICASSO campaign was characterized by periods of stratiform precipitation with embedded convective features, associated with a frontal passage. The 0°C level was located 600 m above ground level (AGL), as indicated by the 7:00 UTC sounding from Larkhill, UK (~35 km west of Chilbolton). Cloud top temperature was approximately –30°C to –35°C, implying that the observed ice formation and growth pathways were dominated by heterogenous processes. FAAM completed roughly eight legs between 5:00 UTC and 10:00 UTC. The distributions of in-cloud N_{FAAM} and $q_{I,FAAM}$ for this flight are presented in Figure 4.1.

We consider in-situ observations and radar gates are collocated if their distance is within 20 km in the horizontal and 1 km in the vertical, and their sample times are within 15 min, based on a nominal wind speed of 10 m s^{-1}. As demonstrated by the black polygon in Figure 4.2, such criteria, coupled with thresholds on the polarimetric variables, help to locate regions of interest for retrieval and evaluation. To ensure meaningful statistics, we further require that each ray contains at least 10 gates, and that each region of interest contains at least three viable rays. Note that radar gates within 150 m of FAAM are eliminated to avoid retrieval contamination by the aircraft.

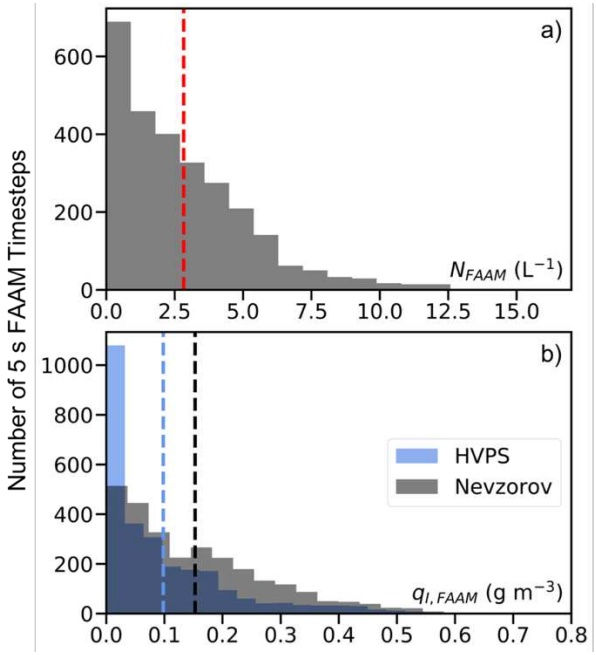

Figure 4.1. (a) Distribution of N_{FAAM} (L^{-1}) for the flight period 5:00 UTC – 10:00 UTC on 13 February 2018. The vertical dashed red line denotes the mean of the distribution. (b) Same as (a), but for $q_{I,FAAM}$ (g m^{-3}). The blue distribution denotes the median $q_{I,FAAM}$ derived from HVPS PSDs using various mass-size relationships in Table 2.2. The grey distribution denotes $q_{I,FAAM}$ from the Nevzorov probe. The vertical dashed blue and grey lines denote the means of similarly colored distributions.

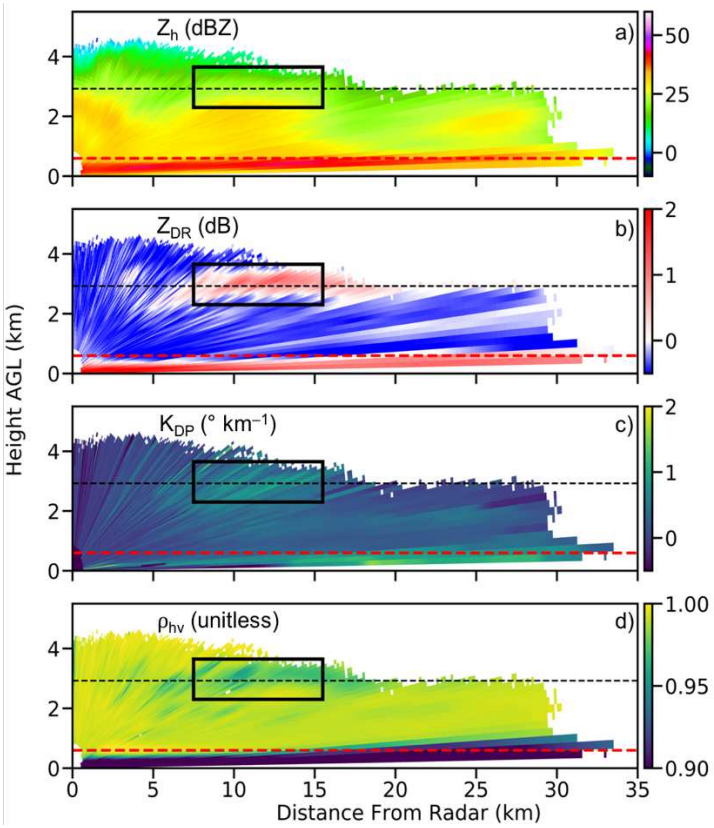

Figure 4.2. Height-distance plots of observed (a) Z_H, (b) Z_{DR}, (c) K_{DP} and (d) ρ_{HV} from the RHI scan at 8:37:25 UTC on 13 February 2018 during the PICASSO field campaign. The red dashed line denotes the 0°C level, while the black dashed line denotes the approximate flight altitude of FAAM during the scan. The black polygon denotes the region that matches the criteria of collocations with FAAM observations and thus is used for retrieval evaluations.

The aforementioned collocation procedure yields 11 cases for evaluation against in-situ observations (Figure 4.3). These cases are comprised of enhanced and spatially homogenous polarimetric signal indicative of the presence of pristine ice crystals ($Z_{\mathrm{DR}} > 0.25$ dB, $K_{\mathrm{DP}} > 0.1$ ° km^{-1}). Figure 4.3(b) depicts that the 25$^{\mathrm{th}}$, 50$^{\mathrm{th}}$ and 75$^{\mathrm{th}}$ percentiles of ENCORE-ICE retrieved N often encompass observed N_{FAAM} for the same or adjacent time periods. Absolute retrieval errors in N are on the order of 16–160%, with only one case exceeding 200% absolute error. Large disagreement between "neighboring" radar scans is likely a function of shifted retrieval regions as dictated by FAAM's change in location in between said scans (~20 s). Figure 4.3(c) shows

that the 25th, 50th and 75th percentiles of ENCORE-ICE retrieved q_I frequently fall within the spread in HVPS-derived $q_{I,FAAM}$. Absolute retrieval errors in q_I exhibit greater variability than that of N and are on the order of 49–500%. Retrieval discrepancies may partially be due to sampling issues, since

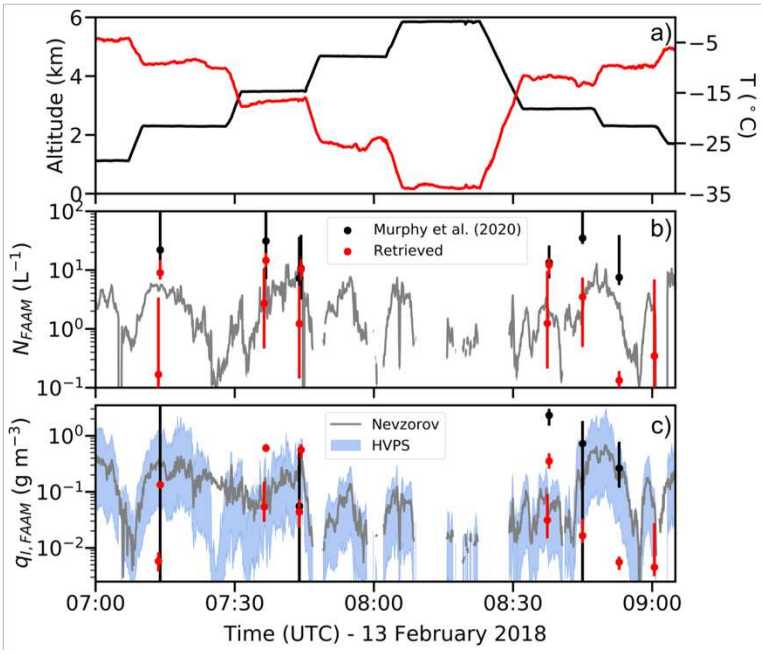

Figure 4.3. Time series of (a) flight altitude (black), temperature (red); observed (black) and retrieved (b) total ice number concentration, and (c) ice water content. Grey shading in (b) denotes instrument uncertainty, while blue shading in (c) denotes uncertainty estimated and bounded by applying various mass-size relationships in Table 2.2 to particle size distributions from HVPS. Retrieval from ENCORE-ICE and Murphy et al. (2020) are denoted by red and black dots, respectively. The dots represent the median of retrieval from all collocated gates, and the vertical bars denote the range between the 25th and 75th percentiles.

the observed N and q_I fluctuate substantially and often vary by an order of magnitude in the span of 10 min.

As a result of this considerable fluctuation and necessarily relaxed collocation thresholds, it is advantageous to compare the distributions of retrieved N and q_I for all gates considered against the distributions of N_{FAAM} and $q_{I,FAAM}$ for the time period in question (~7:00–9:00 UTC).

Figures 4.4 and 4.5, respectively, depict these distributions as well as that from Murphy et al. (2020) for the same radar rays used in ENCORE-ICE. For all cases considered, the 25th, 50th, and

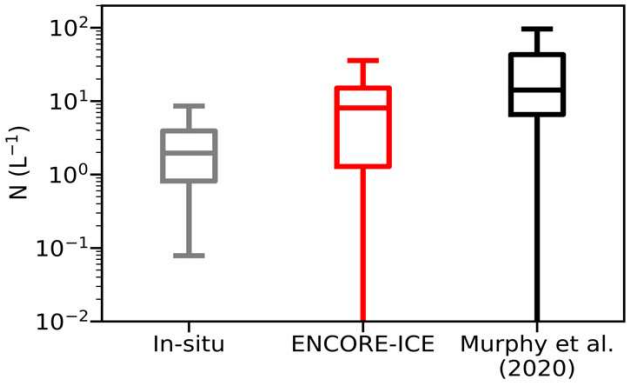

Figure 4.4. Distributions of N_{FAAM} (grey) for 7:00–9:00 UTC and ENCORE-ICE (red) and Murphy et al. (2020) (black) retrieved N for the 11 cases shown in Figure 4.3.

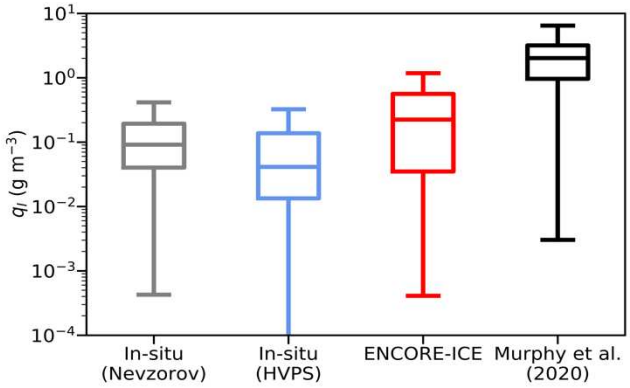

Figure 4.5. Distributions of Nevzorov (grey) and HVPS-derived (light blue) $q_{I,FAAM}$ for 7:00–9:00 UTC and ENCORE-ICE (red) and Murphy et al. (2020) (black) retrieved q_I for the 11 cases shown in Figure 4.3.

75th percentiles of ENCORE-ICE retrieved N are 1.3 L^{-1}, 8.1 L^{-1}, and 15.1 L^{-1}, respectively. Between 7:00–9:00 UTC, the 25th, 50th, and 75th percentiles of N_{FAAM} are 0.8 L^{-1}, 2.0 L^{-1}, and 3.9 L^{-1}, respectively. While we generally overestimate N relative to N_{FAAM}, there is considerable overlap between the two distributions, as seen in Figure 4.4. Murphy et al. (2020) similarly

overestimates N, but its distribution exhibits considerably less overlap relative to N_{FAAM}. Similarly, the 25th, 50th, and 75th percentiles of ENCORE-ICE retrieved q_I are 0.04 g m^{-3}, 0.22 g m^{-3}, and 0.56 g m^{-3}, respectively. For Nevzorov $q_{I,FAAM}$, they are 0.04 g m^{-3}, 0.09 g m^{-3}, and 0.19 g m^{-3}, respectively. We observe better overlap between ENCORE-ICE retrieved and observed distributions of q_I, with Murphy et al. (2020) exhibiting no overlap and having a median q_I that is approximately an order of magnitude larger than the observed median from either $q_{I,FAAM}$ sources. The overestimation in retrieved N and q_I from ENCORE-ICE and Murphy et al. (2020) can also be partially attributed to the aforementioned polarimetric thresholds applied for case selection.

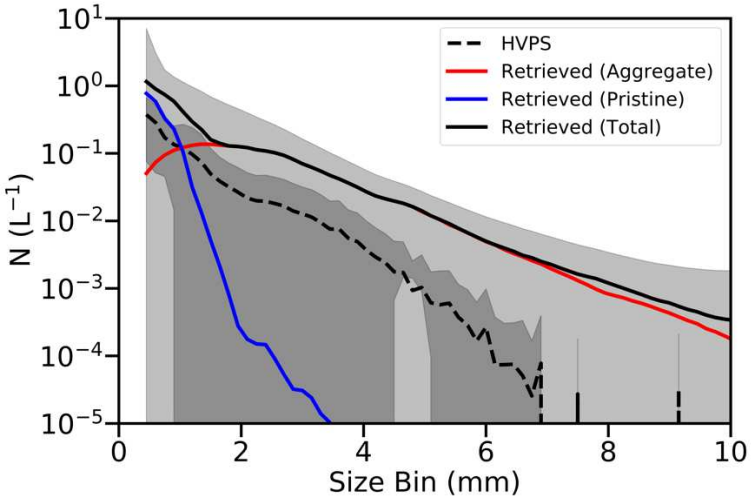

Figure 4.6. Median retrieved particle size distributions for the 8:37:25 case in Figure 4.3 and denoted in Figure 4.2. Blue denotes that of pristine ice, red denotes that of aggregates, and solid black denotes the total particle size distribution. Dashed black denotes the mean in-situ particle size distribution for collocated timesteps. Grey shading about the dashed and solid black lines denotes one standard deviation of the total retrieved and in-situ distributions.

As previously stated, we compare retrieved PSDs against their in-situ counterparts in an effort to diagnose these discrepancies. Figure 4.6 depicts the median retrieved PSDs for pristine

ice and aggregates, as well as the total retrieved PSD for the case at 8:37:25 UTC. The observed PSD appears to be modestly bimodal, with a secondary peak in number concentration at ~3 mm. Such PSD behavior is frequently observed in midlatitude stratiform ice clouds (e.g. Field et al. 2005) and is typically attributed to snow aggregation (Westbrook 2004a,b). In retrieving independent size distributions for pristine ice and aggregates, we are able to capture such bimodality if and when it exists. Figure 4.6 demonstrates this, as indicated by the parralel nature between the observed and retrieved total PSDs. However, it is apparent that we overestimate aggregate N in this case, as our retrieved total PSD is shifted ~0.5–1 order of magnitude at each size bin. This finding helps to explain our modest positive bias in N (~17%) and q_I (~79%) relative to FAAM observations for this case. Further investigation is necessary to determine whether this aggregate overestimation is systematic and if there are ways to constrain it.

While direct collocation is preferred, concessions were necessary to ensure a sufficient number of data points per case for evaluation with the limited data available. Further efforts towards validation using data where deliberate radar-aircraft collocation was attempted would enhance confidence in these results. Based on the degree of variability evident in the in-situ data (Figure 4.3(b,c)), direct comparisons of statistical values (i.e. mean/median) across such large spatiotemporal windows may compound the errors outlined above. Interestingly enough, if our retrievals are shifted ~10-15 minutes in time (within the previously defined temporal collocation threshold), the agreement between in-situ (and Murphy et al. 2020), is considerably better in some cases. It is possible that, while the in-situ timesteps fall within our collocation thresholds, that FAAM did not actually sample the microphysical environment responsible for the polarimetric signatures present in our identified cases until later in time, leading to such a time lag.

4.2 Spatiotemporal evolution of cloud ice number concentration using BAECC data

4.2.1 19 August 2014

The atmospheric environment of 19 August 2014 from the BAECC campaign can be described as post-frontal, with isolated precipitation between 0:00 UTC and 12:00 UTC with precipitation rates of ~5–10 mm hr^{-1}. The 0°C level was located 2160 m AGL and cloud top temperature ranged from approximately –38°C to –15°C. This case differs from the PICASSO case discussed in Section 4.1 because embedded convective features are more apparent and the precipitation echo tops extend 1-3 km higher, varying considerably and implying stronger vertical motion. Figure 4.7 depicts the evolution of the precipitation field from 0:00 UTC to 12:00 UTC, as observed by the Ka-band zenith-pointing radar (KAZR) and the collocated weighing bucket rain gauge. We will first discuss retrieval results from a snapshot (~4:34:20 UTC) during the scan denoted by the red horizontal bar in Figure 4.7. This case directly follows the period of strongest precipitation, after which the cloud top height has decreased from ~7.5 km to ~5 km.

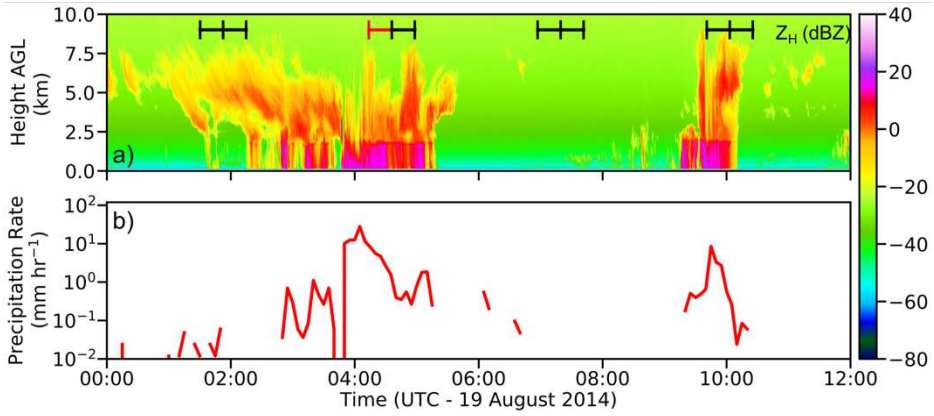

Figure 4.7. Time–height plots of observed (a) attenuated Z_H from the ARM vertically pointing radar at 37 GHz and (b) precipitation rate (mm hr^{-1}) from rain gauge on 19 August 2014. The horizontal black bars in (a) represent the time period of XSACR along-wind RHI scans throughout the day. The red horizontal bar denotes the scan for case studies in Section 4.2.1.

Figure 4.8 depicts the scan for the time period directly proceeding the relatively heavy precipitation and during what appears to be the temporary decay of the cloud field. The hydrometeor classification for this scan using a radar-based fuzzy logic scheme based on hydrometeor scattering calculations (Dolan et al. 2013) is shown in Figure 4.9, while the horizontally-averaged vertical profiles of radar observables for the region of interest (denoted by the black polygon) is shown in Figure 4.10. As shown in Figure 4.8, this scan encompasses a widespread region of collocated $Z_{\mathrm{DR}} > 1$ dB, $K_{\mathrm{DP}} > 0.5$ ° km^{-1} and depressed ρ_{HV}, indicative of the potential that pristine ice is embedded in snow aggregates. This is the main reason why we select this scan to illustrate retrieval performance.

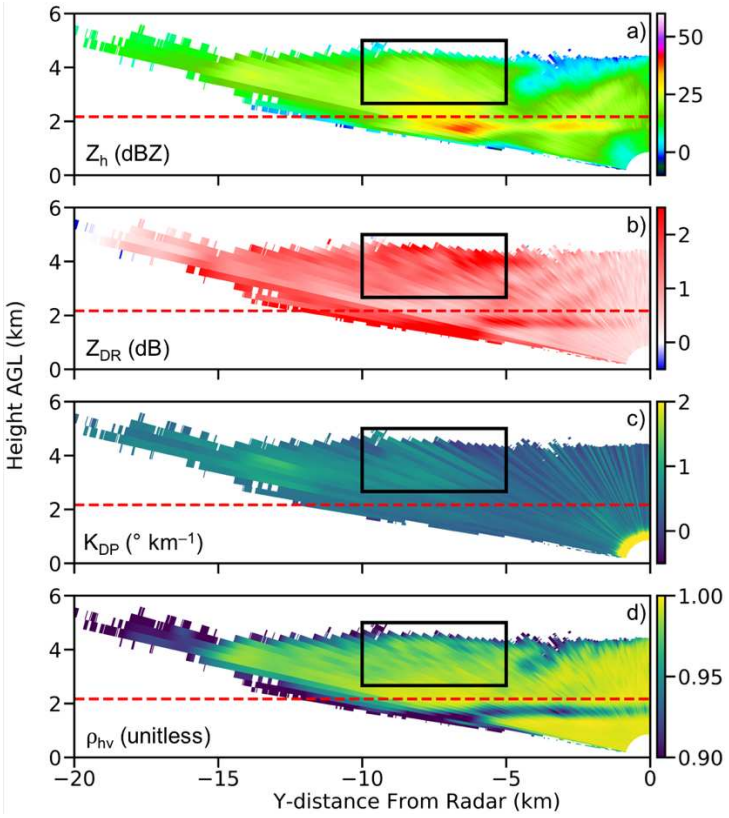

Figure 4.8. Range-height scans of observed (a) Z_H, (b) Z_{DR}, (c) K_{DP}, and (d) ρ_{HV} at 4:13:39 UTC on 19 August 2014 during the BAECC field campaign. The red dashed line denotes the 0°C level and the black polygon denotes the region for retrieval.

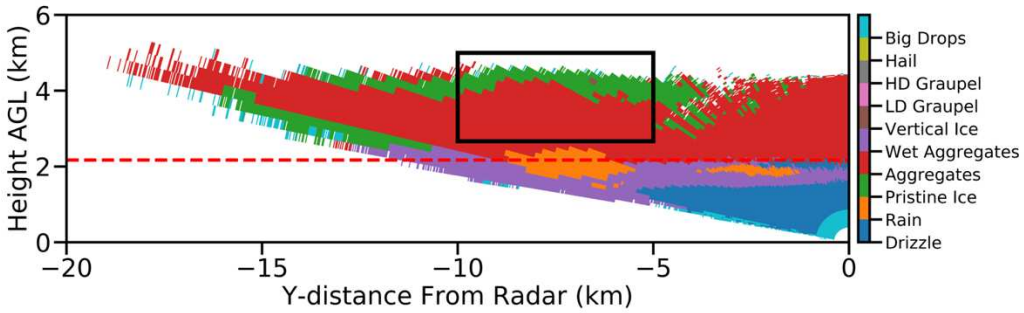

Figure 4.9. Range-height plot of most likely hydrometeor types indicated by a radar-based fuzzy logic hydrometeor classification scheme (Dolan et al. 2013). The red dashed line denotes the 0°C level and the black polygon denotes the region for retrieval. Green shading denotes regions of pristine ice whereas red shading denotes regions of snow aggregates.

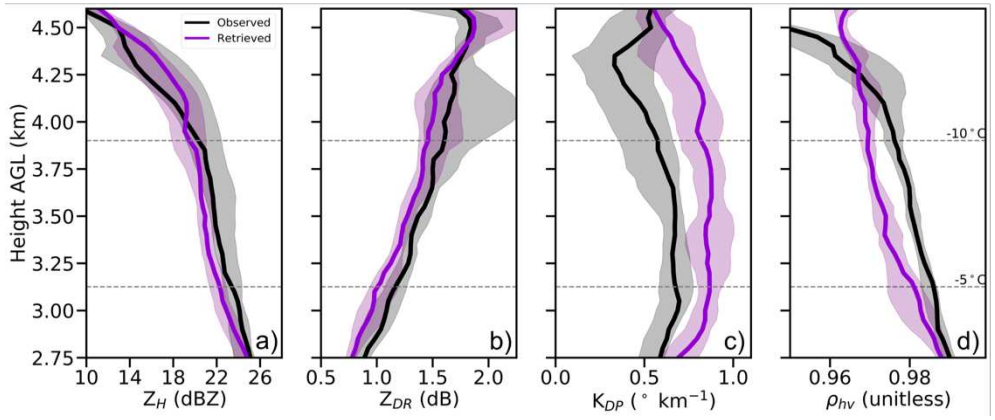

Figure 4.10. Vertical profiles of observed and retrieved (i.e. simulated by our forward model) (a) Z_H, (b) Z_{DR}, (c) K_{DP}, and (d) ρ_{HV}, averaged from radar gates that were linearly interpolated to a 50 m x 50 m x 50 m grid in the region denoted in Figure 4.8. Grey shading and purple shading are bounded by their 25th and 75th percentiles. Black dashed lines denote the temperature levels of –5 and –10°C.

Near cloud top (~4.5 km AGL) in this region, Figure 4.9 indicates pristine ice as the likely dominant hydrometeor type. Recall that pristine ice particles can yield Z_{DR} of several dB because of their aspect ratios and preferential horizontal orientation. Thus, the peak of Z_{DR} at ~4.5 km AGL in Figure 4.10 is consistent with the hydrometeor type suggested in Figure 4.9. Additionally, the Z_{DR} peak is in a temperature zone between –12°C and –15°C, known as the dendritic growth zone, where pristine ice growth is thermodynamically maximized, supporting

the presence of pristine ice in this region. In contrast, from cloud top down to just above the melting layer (~2.5 km), Z_{H} and ρ_{HV} both increase while Z_{DR} decreases in Figure 4.10, suggesting a transition in the dominant hydrometeor type from pristine ice to aggregates, as shown in Figure 4.9. This type of vertical structure with pristine ice growth aloft and aggregation below has been observed in many studies (e.g., Kennedy and Rutledge 2011; Andric et al. 2013; Bechini et al. 2013; Kumjian et al. 2014; Oue et al. 2015), indicating the representativeness of our selected case for ice- and mixed phase clouds.

To evaluate our retrieval, we first examine whether the forward-modeled radar observables agree with the observations. Figure 4.10 shows that the mean modeled profiles of Z_{H} and Z_{DR} generally fall within the observational uncertainty, indicating that forward models for these variables work properly and retrievals are reasonable. Importantly, the observed and modeled mean profiles have similar variations with respect to height. However, the agreement in K_{DP} and ρ_{HV} profiles is less satisfactory and shows systematic high and low biases, respectively, in the cloud layer between –5 and –10°C. The bias in ρ_{HV} would suggest that we overestimate the degree of the heterogeneity in radar sample volumes, meaning that we either overestimate pristine ice contributions in an aggregate-dominant region, or overestimate aggregate contributions in a pristine ice dominant region. The modest positive bias in K_{DP} would support the overestimation of pristine ice contributions in an aggregate-dominant region. If the opposite was the case (i.e. an overestimation of aggregate contributions), then the agreement in Z_{H} and Z_{DR} would be considerably worse, as these variables are much more sensitive to aggregates than pristine ice, owing to their larger sizes. However, it is also true that observing and modeling ρ_{HV} are both challenging, and that finer instrument calibration issues could contribute to this error. The observed errors in ρ_{HV} are on the order of the observational uncertainty given in Table 3.2.

As such, reconciling this disagreement and potential bias would require improvement in instrument calibration and scattering database, which is out of the scope of the study. While systematic disagreement between observed and simulated ρ_{HV} is worthy of concern, we have found that the inclusion of ρ_{HV} as part of the observation vector remains crucial, and retrieval skill does not seem to degrade because of the potential bias in ρ_{HV}.

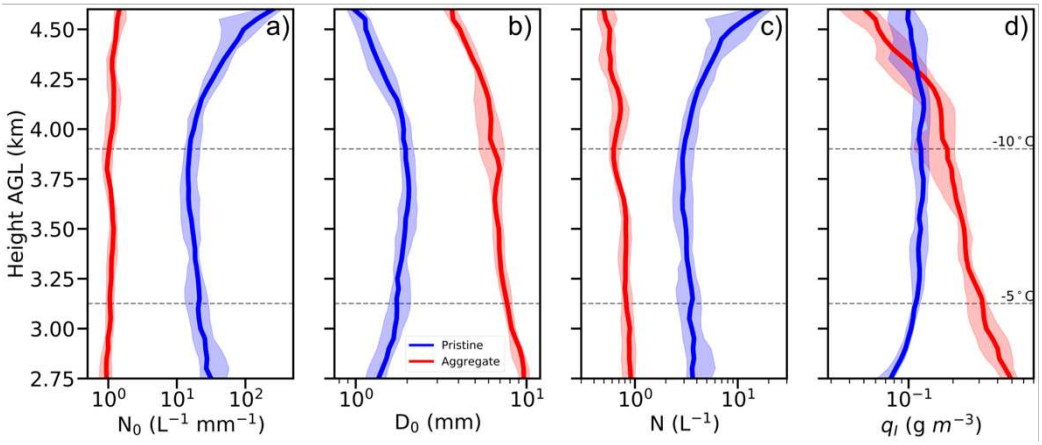

Figure 4.11. Same as Figure 4.10, but for ENCORE-ICE-retrieved (a) N_0, (b) D_0, (c) N, and (d) q_I. Solid blue and red lines denote retrievals for pristine ice and snow aggregates, respectively, with shading in their own color is bounded by the 25$^{\mathrm{th}}$ and 75$^{\mathrm{th}}$ percentiles of profiles.

Figure 4.11 shows the horizontally-averaged vertical profile of pristine ice and aggregates retrieved from ENCORE-ICE. As expected, Figures 4.11(c,d) indicate that the total number concentration N is dominated by pristine ice, while in contrast, the total ice water content q_{I} is dominated by aggregates. The pristine ice number concentration (N_{P}) is ~4 L^{-1}, approximately 4.5 times larger than that of aggregate (N_{A}). DeMott et al. (2010) predicts an activated INP, or potential pristine ice, number concentration of 0.002–0.27 L^{-1} whereas Schneider et al. (2020) predicts 0.0001–0.05 L^{-1}, with the upper/lower bounds of these ranges corresponding to the coldest/warmest temperatures in the region of interest. N_{P} remains relatively constant up to ~4.25

km, where it then increases rapidly with height afterwards. Pristine ice is likely nucleating around cloud top at temperatures near –15°C, as indicated by the maxima in N_{P}. These are likely young pristine ice crystals with smaller maximum dimensions, as $D_{0,P}$ tends to be small and peaks near ~3.8 km with median volume diameter of 1.75 mm and coincident peak in ice water content. This would imply that these crystals are growing as they fall. The number concentration of aggregates (N_A), ranging between 0.5 L^{-1} to 1.0 L^{-1}, shows a modest decrease with height, as expected. Clearly, the size of aggregates generally increases from ~5 mm to ~10 mm from the pristine-dominant region towards the ML, determining the shape of the vertical profile of $q_{I,A}$ and supporting the notion that aggregation is occurring at temperatures warmer than –12°C to –10°C.

While the shape of the vertical profiles are in agreement, we observe a modest, consistent overestimation of N and underestimation of q_I (Figures 4.12(a,b), respectively), relative to what is expected from Murphy et al. (2020). These findings provide further evidence that we may be modestly overestimating pristine ice at the expense of aggregates for this case, as pristine ice is expected to be the dominant control on fluctuations in N, while aggregates would be the dominant control on q_I even in low concentrations. Retrieved pristine ice and aggregate D_0 straddle that from Murphy et al. (2020) (Figure 4.12c). This is to be expected, as we are comparing D_0 of independent PSDs (pristine ice skewed towards smaller sizes, aggregates towards larger) against a bulk D_0. If one was to combine independent pristine ice and aggregate PSDs, it is likely that the resultant retrieved bulk D_0 would fall between the D_0 of respective independent PSDs. In light of the disagreement in forward-modeled K_{DP}, potential overestimation of pristine ice N, and comparison against expected values from DeMott et al.

(2010) and Schneider et al. (2020), we elect not to hypothesize whether SIP may have been active during this case.

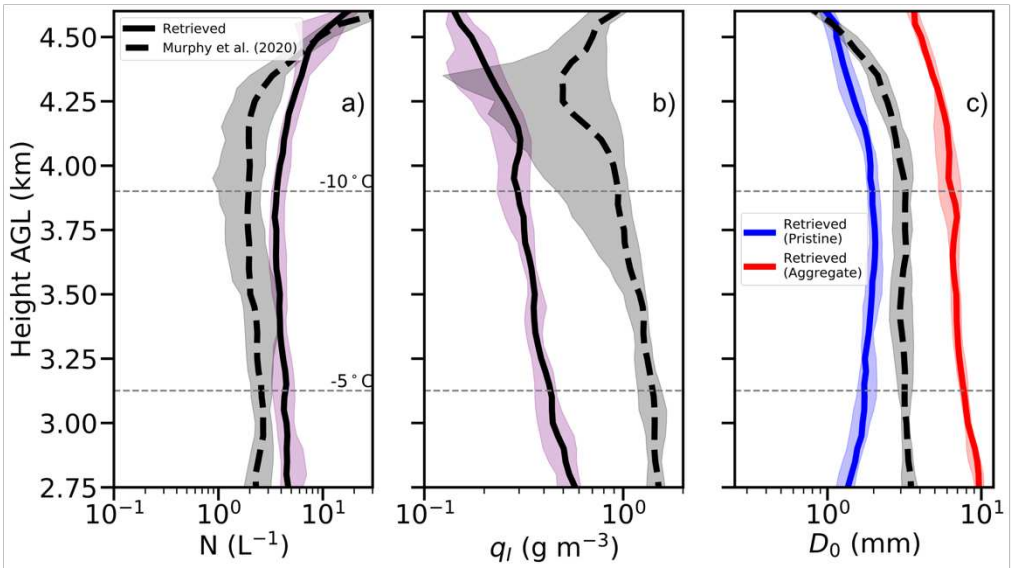

Figure 4.12. Same as Figure 4.11, but estimates from empirical relationships described in Murphy et al. (2020) are co-plotted. (a) N, (b) q_I, and (c) D_0. Black dashed lines denote estimates from Murphy et al. (2020). Black solid lines in (a) and (b) denote ENCORE-ICE-retrieved total N and q_I (i.e. the sum of pristine ice and aggregates). Retrieved D_0 of pristine ice and aggregates in (c) are denoted respectively by blue and red lines. Shading in their own color is bounded by the 25th and 75th percentiles of profiles.

4.2.2 18 August 2014

Unlike the previous case that is characterized by intermediate K_{DP} values (approx.. 0.3–0.6° km^{-1}), the case on 18 August 2014 is associated with moderately enhanced K_{DP} (> 1.0 km^{-1} at times), implying the presence of pristine ice crystals in larger concentrations. This allows us to examine the sensitivity of our retrieval to such enhancements and speculate whether SIP has occurred. That is, whether the corresponding pristine ice number concentration exceeds the predicted primary ice N by orders of magnitude. As this case is a day before the previous case, a frontal system was passing through the site. Comparison of the two days also provides an

opportunity to further examine the predominant ice microphysical characteristics of frontal and post-frontal cloud systems. Radiosondes launched at Hyytiälä indicate backing winds with height and subsequent cold air advection associated with the frontal passage. Between 0520 UTC and 2321 UTC, the 0°C level lowered from ~2.5 km to ~2.3 km and the –15°C level lowered from ~5.1 km to ~4.7 km. Similar to Figure 4.7, Figure 4.13 depicts the evolution of the precipitation field over the course of the day, as observed by KAZR and rain gauge. Compared to 19 August 2014, the current case has more persistent precipitation with a mixture of moderate and heavy precipitation rates. For this case, cloud top temperatures were similarly as low as approximately –38°C, but were generally colder, typically near –25°C.

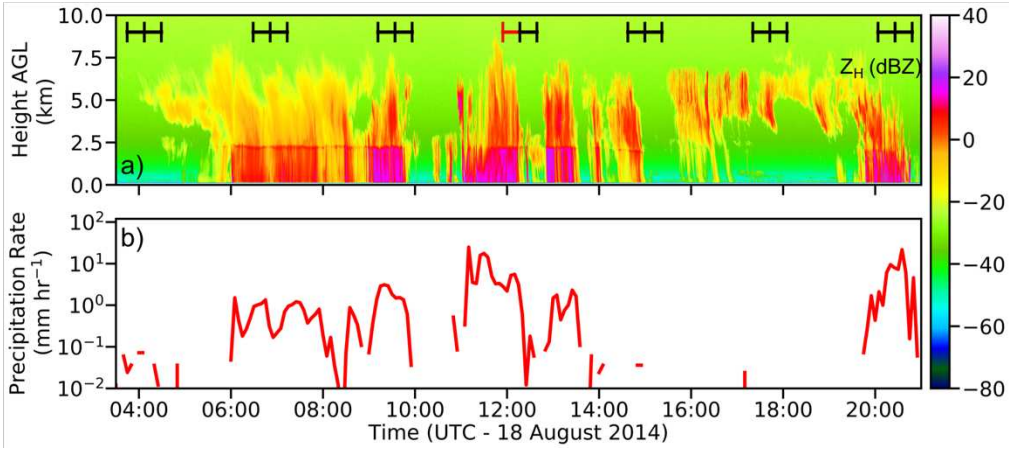

Figure 4.13. Same as in Figure 4.7, but for 18 August 2014. The red horizontal bar in (a) denotes the 11:54:29 UTC XSACR along-wind RHI scan discussed in Section 4.2.2.

Figure 4.14 depicts the polarimetric observables for the scan at ~12 UTC. Contrary to Figure 4.8 discussed in Section 4.2.1, cloud top extends an additional 2–2.5 km vertically and is subsequently associated with lower temperatures (< –25°C). As indicated in Figure 4.16, this case has generally similar Z_{H} and ρ_{HV}, but higher K_{DP}. Specifically, we can see that K_{DP} can be larger than the previous case by a factor of 2, as indicated by its distribution's longer positive tail

in Figure 4.15. The lower cloud top temperature and higher K_{DP} associated with this period support the possibility of higher pristine ice N.

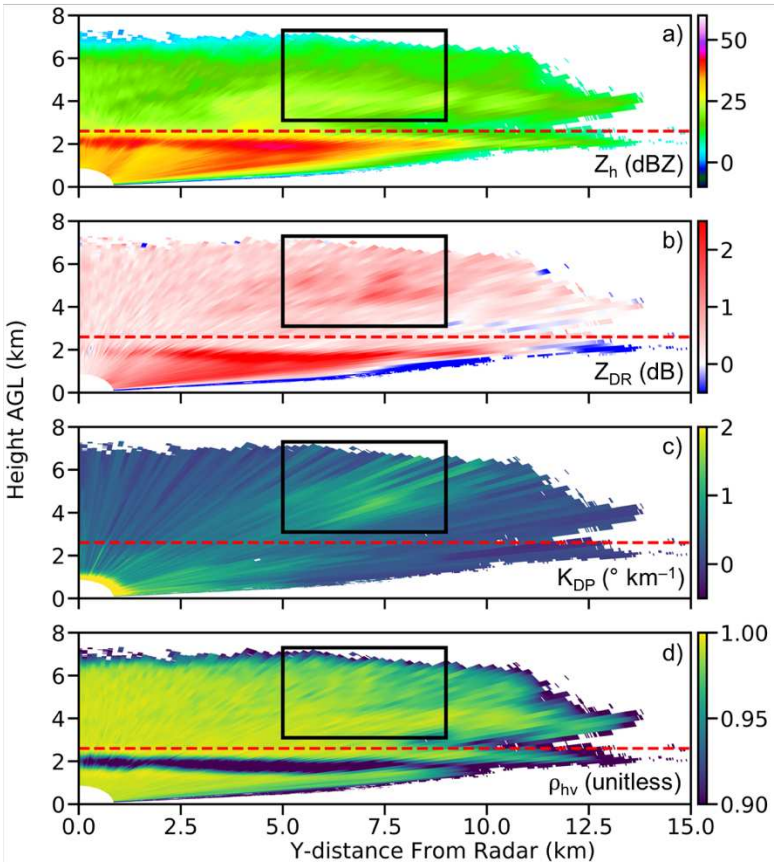

Figure 4.14. As in Figure 4.8, but for the 18 August 2014 11:54:29 RHI scan.

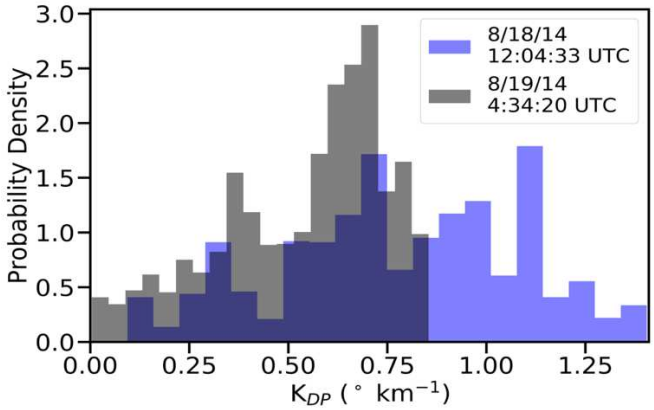

Figure 4.15. Distribution of K_{DP} for the respective regions of interest denoted in Figures 4.8 (grey) and 4.14 (blue).

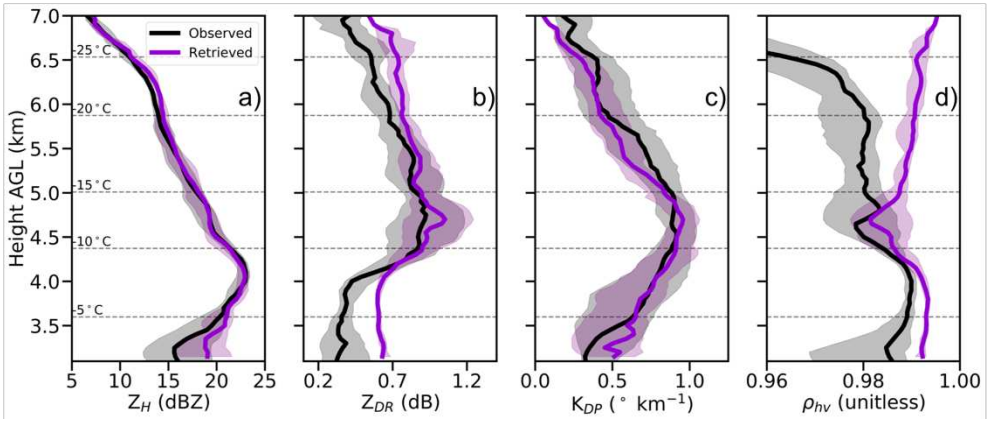

Figure 4.16. As in Figure 4.10, but for the 18 August 2014 11:54:29 RHI scan.

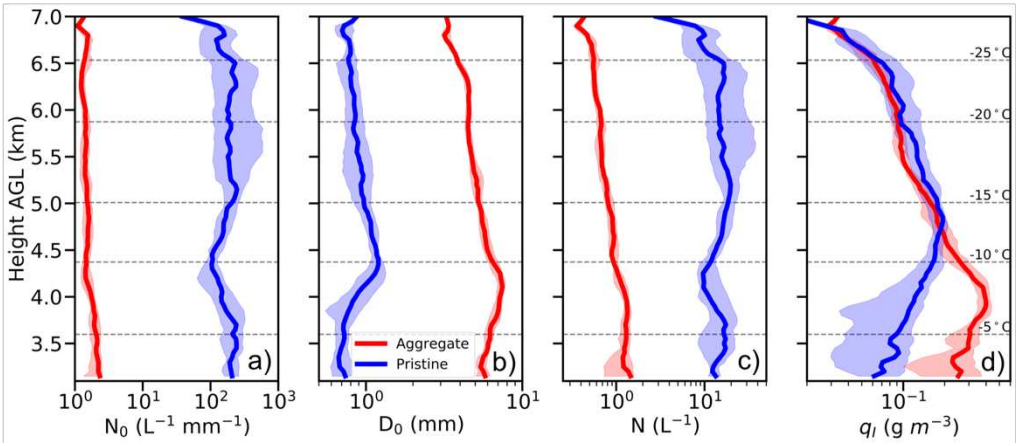

Figure 4.17. As in Figure 4.11, but for the 18 August 2014 11:54:29 RHI scan.

Figure 4.16 depicts better agreement between forward-modeled observables in both the mean profile shape and horizontal variability than in the previous case. There is particular improvement in K_{DP} relative to the previous case, but errors in ρ_{HV} persist. However, these errors are again on the order of uncertainty in ρ_{HV} throughout the majority of the column. We see considerable divergence in ρ_{HV} near cloud top when Z_{H} drops below ~10 dBZ. Such precipitous drop off in ρ_{HV} near cloud top has been identified before (Keat and Westbrook 2017) and is a manifestation of degraded radar signal quality due to sparse hydrometeor populations. As such, this feature is likely not physical and our inability to model it is not of concern. Nonetheless, such features can (and will need to be) corrected in order to retrieve microphysical properties near cloud top moving forward.

The combination of better agreement in K_{DP} and good agreement in Z_{DR} for this case should imply greater confidence in our retrieved pristine ice N. As seen in Figure 4.17, retrieved pristine ice N is between 10–30 L^{-1} and pristine ice q_I is between 0.06–0.2 g m^{-3} through the depth of the column, but drop off considerably towards cloud top. Between –5°C and –15°C, retrieved pristine ice N for this case is ~2–3 times the retrieved pristine ice N presented in Section 4.2.1 for the same temperature range. This difference may be even higher, considering the potential overestimation of pristine ice N in Section 4.2.1. Figure 4.18 indicates that, for this temperature range, DeMott et al. (2010) predicts an activated INP, or potential pristine ice, number concentration of 0.097–0.37 L^{-1} whereas Schneider et al. (2020) predicts 0.006–0.07 L^{-1}.

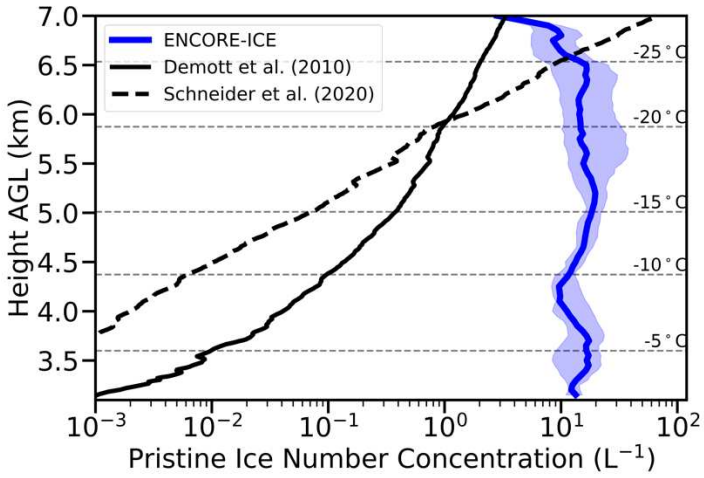

Figure 4.18. As in Figure 4.17c, with expected primary ice number concentration from DeMott et al. (2010) and Schneider et al. (2020) coplotted in solid black and dashed black, respectively.

Taking DeMott et al. (2010) as the conservative (i.e. larger) value, this would correspond to a retrieved enhancement in pristine ice N of at least ~1–3 orders of magnitude relative to what is expected via primary ice nucleation. It is worth noting that our retrieved pristine ice N agrees quite well with expected values near cloud top. Prior to making assertions about SIP lower in the cloud, it is necessary to eliminate alternative sources for this enhanced pristine ice N, such as seeding from near cloud top (e.g. Moisseev et al. 2015). The hydrometeors near cloud top do not appear to be sedimenting, as indicated by near 0 m s^{-1} vertical velocities observed by KAZR near cloud top during this time period. In this context and based upon the traditionally accepted definition of SIP, this region may be undergoing SIP. We have higher confidence in this assessment of SIP based upon the better agreement between the observed and forward-modeled variables compared to the previously discussed case. These results are encouraging, as it demonstrates the retrieval framework's sensitivity to K_{DP}, ability to identify regions of enhanced pristine ice N, and thus its utility for establishing climatologies of pristine ice N and in the surveillance of SIP events. Furthermore, good agreement with expected values near cloud top

imply that the retrieval framework could be useful for evaluating aerosol-based primary ice N parameterizations and improving the understanding of aerosol controls on ice phase microphysics.

4.2.3 Example of time series

As mentioned in Chapter 2, one of the unique aspects of the BAECC campaign is the availability of consistent along-wind radar scans, which allows us to study pristine ice number concentration in a Lagrangian sense. Following the confidence gained in the previous case studies, Figure 4.19(a) shows a time series of retrieved N_{P} associated with the case in Section 4.2.2, where SIP is hypothesized to have occurred. Predicted primary ice number concentrations for investigating the temporal variation of N_{P} is also plotted to assist in this investigation. The retrieved N_{P} ranges between ~3–100 L^{-1}, with a mean and standard deviation of 12.7 and 1.1 L^{-1}, respectively. Compared to N_{A} that has a mean and standard deviation of 1.0 and 0.1 L^{-1}, respectively, N_{P} is typically 10 times larger than N_{A}. The range and variation of N_{P} in Figure 4.19(a) are larger than those observed by in-situ measurements (2.6 ± 2.1 L^{-1}) during the PICASSO campaign (Figure 4.1), and those (0–40 L^{-1}) by in-situ measurements reported in Murphy et al. (2020) for the trailing stratiform region of a mesoscale convective system (Figure 2.3(a)) .

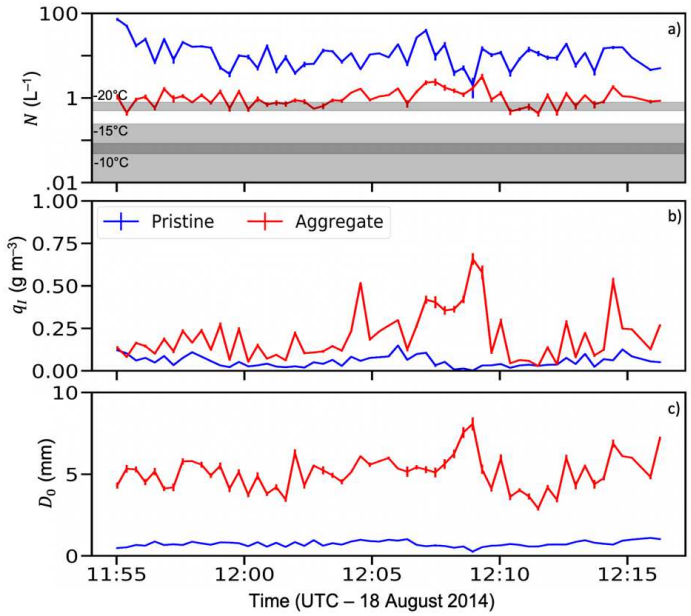

Figure 4.19. Time series of mean (a) N, (b) q_I, and (c) D_0 between –5°C and –20°C for the 18 August 2014 11:54:29 RHI scan. Blue lines denote pristine ice and red lines denote aggregates, with vertical bars representing one standard deviation. Grey shading in (a) denotes the upper and lower bounds of predicted N using DeMott et al. (2010) and Schneider et al. (2020) for –10°C, –15°C, and –20°C. The darker grey shading denotes overlap between the upper bound at –10°C and lower bound at –15°C.

As discussed in Section 2.2.2, the predicted primary ice number concentration is highly dependent on the ambient temperature. Since the radar gates span a temperature zone from –5 to –20°C, we calculate the predicted primary ice number concentrations N_{INP} from DeMott et al. (2010) and Schneider et al. (2020) for –5°C, –10°C, –15°C, and –20°C and compare against the values in Figure 4.19(a). Predicted N_{INP} for –5°C is order 10^{-3} L^{-1} and not plotted. Taking the conservative (i.e. largest) prediction from a temperature of –20°C, Figure 4.19(a) shows that retrieved N_{P} is nearly always at least 0.5 orders of magnitude greater than predicted N_{INP} and frequently exceeds 1–2 orders of magnitude in excess predicted N_{INP}. If we define that an SIP event as N_{P} of at least 100 times larger then it is difficult to confidently say SIP is occurring. However, if we consider predicted N_{INP} at a temperature of –15°C, the temperature regime

associated with frozen drop mechanisms (Phillips et al. 2018) of SIP, it can be said with reasonable confidence that SIP is occurring more often than not, due to the persistently elevated retrieved N_{P}. However, further investigation is necessary to confirm this hypothesis.

Figures 4.19(b,c) show the evolution of q_I, and D_0, respectively. The mean aggregate D_0 of ~4–8 mm is consistent with the range reported in literature (e.g., Tiira et al. 2016) and is generally larger than pristine ice by a factor of 7. Similar to results of the case studies, even though aggregates have much smaller number concentrations, their large sizes lead to dominance in total q_I, as shown in Figure 4.19(b). Note that all retrieved properties demonstrate variability from timestep to timestep. Such variations are unlikely real and require further investigation to identify the responsible sources. To create such time series, a box that advects with the mean wind field is used to define the retrieval region at each timestep. To reduce computational cost, the 10 "strongest" polarimetric signatures (dictated by Z_{DR} and K_{DP}) within this region for each timestep are retrieved. The relatively small number of gates (500-1000), coupled with these "jumps" from ray to ray, may explain this variability.

Interestingly, a significant peak in aggregate D_0 and q_I occurs around ~12:07 UTC, which is near the time period of enhanced surface precipitation rates (Figure 4.13(b)). This peak is preceded by several timesteps of consistent increase, which may imply that there are physical mechanisms responsible, rather than purely internal variability in the retrieval. Nonetheless, it is possible that we are observing an isolated signature of enhanced aggregation aloft correlated with stronger surface precipitation rates. However, further analysis is required to identify potential time lags based on the radar signature's location relative to the surface rain gauge and prevailing wind field.

In short, while the relative enhancement in ice number concentration from this scan period is sensitive to the temperature zone considered, the comparison with the predicted primary ice number concentration suggests some multiplication processes may be present at temperatures warmer than –15°C. More detailed retrieval partitioning and knowledge of the cloud evolution is necessary to make additional conclusions on the validity of our SIP claims. Furthermore, while the preeminent goal is the documentation of pristine ice microphysical evolution, the identification of potential enhanced aggregation aloft indicates that we may be able to link microphysical processes to surface precipitation evolution (an unforeseen positive outcome).

CHAPTER 5

Summary, Conclusions, and Future Work

5.1 Summary and conclusions

Clouds are dominant controls on global precipitation distribution and radiative balance. Clouds containing ice are of particular importance, because they are responsible for the majority of precipitation globally and their optical, and thus radiative, properties are unique relative to liquid clouds. Over the past 30 years, observations and retrievals of liquid clouds have experienced a renascence. While progress has been made in the realm of ice and mixed-phase clouds, it lags considerably, due to the inherent complexity of ice microphysical processes and their outcomes. As such, novel platforms for surveilling these clouds and retrieving relevant microphysical parameters are of great importance for improving our understanding of the processes at work and thus better informing their representation in microphysics parameterizations.

Here, we contribute to filling this gap by developing a framework for simultaneously retrieving microphysical properties of pristine ice and snow aggregates using polarimetric radar data. By extension, their individual contributions to the bulk cloud ice number concentration and ice water content can be obtained. Based on limited evaluation using the PICASSO data, we demonstrate that our retrieval is superior to the existing method that estimates ice number concentration from empirical relationships. The two-hour PICASSO flight used in evaluations show great variations in both ice water content (0.01–1 g m^{-3}) and ice number concentration (0.1–10 L^{-1}). The median retrieved ice water content of 0.22 g m^{-3} falls well within the observed

range, while the median retrieved ice number concentration of 8.1 L^{-1} is on the higher end of the observed distribution. For comparison, the existing method (Murphy et al. (2020)) has yielded ice water content of 2.3 g m^{-3} and ice number concentration of 13.4 L^{-1}. The results for the presented PICASSO cases suggest that we may overestimate aggregate contributions to number concentration, leading to overestimation in ice water content.

Compared to PICASSO, radar data from BAECC tend to have higher polarimetric signal and are less noisy. Capitalizing on good quality data, we were able to characterize the instantaneous vertical structure of ice microphysical properties at temperatures colder than –5°C and quantitatively linking them to observed polarimetric "fingerprints" associated with common ice microphysical processes such as pristine ice nucleation, aggregation, and potentially secondary ice production. Our results confirm that the ice water content is mainly dictated by aggregates, while the ice number concentration is mainly modulated by pristine ice. For the BAECC cases, retrieved ice number concentration tends to be higher than that found in the PICASSO campaign, while the average ice water content from two campaigns are rather similar (~0.5 g m^{-3}). Retrieved ice number concentration is generally well above the predicted primary ice number concentration using ambient temperatures >= –15°C, indicating that SIP processes may be at play, but further analysis is warranted to increase our confidence in this assertion.

5.2 Future work

Future work falls under two umbrellas: improving the retrieval and applying it to a greater wealth of data for discovering robust statistics on secondary ice productions events.

While our retrieval appears to be physically reasonable and outperforms the existing method in comparison with in-situ measurements, the difference between the observed and retrieved ice number concentrations remains large and not ideal. Though the difference can

partly be attributed to the sampling issue considering the closest distance of 5 km between radar gate and FAAM aircraft and our focus on cases with enhanced polarimetric signatures, further evaluation and improvement is needed. First, data quality of in-situ measurements requires further clarification from the data provider, because ice water content in the recent version has been reduced significantly, and there is no documentation yet to explain what justification such a reduction is based on. Second, collocated data points exist at other timesteps and will be examined carefully. If the retrieved ice number concentration remains systematically higher as shown in Section 4.1, we plan to examine if any further constraints in the prior are needed. The potential constraints include 1) a pre-defined vertical profile in particle size that uses radar observables as the foundation of the first guess and 2) applied smoothness in the state vector vertical profiles that is representative of what is observed in nature. However, care must be taken in 1), as introducing such correlations requires more advanced retrieval equations. We also intend to rigorously test the sensitivity of our retrieval to the choice of prior and spread in our initial state. It is rather important to reduce the high bias in pristine ice number concentration, because this microphysical property is the key variable used to identify SIP events.

As alluded to previously, the preeminent goal of this work is to use the new retrieval method to identify SIP events, document their spatiotemporal evolution, and evaluate their impact on the larger cloud structure and precipitation properties at the surface. To do so first requires a climatological characterization of ice microphysical properties, particularly pristine ice number concentration, across the entire BAECC campaign. In doing so, SIP events can be identified through the deviation of pristine ice number concentration from this climatology. Once SIP events are identified, their latent atmospheric environments can be examined to investigate the required atmospheric conditions and underlying mechanisms necessary to initiate and support

these SIP events. These derived relationships can be further decomposed to assess which primary SIP mechanisms are predominant under certain atmospheric conditions. This new information will then be compared against existing knowledge of these processes. Any novel information will be pursued further, and attempts will be made to incorporate it into existing modelling frameworks to quantify its impact on cloud structure, precipitation, and radiation properties.

REFERENCES

Abel, S. J., R. J. Cotton, P. A. Barrett, and A. K. Vance (2014), A comparison of ice water content measurement techniques on the FAAM BAe-146 aircraft, *Atmospheric Measurement Techniques*, *7*(9), 3007–3022, doi:10.5194/amt-7-3007-2014.

Andrić, J., M. R. Kumjian, D. S. Zrnić, J. M. Straka, and V. M. Melnikov (2013), Polarimetric Signatures above the Melting Layer in Winter Storms: An Observational and Modeling Study, *Journal of Applied Meteorology and Climatology*, *52*(3), 682–700, doi:10.1175/jamc-d-12-028.1.

Aydin, K., and T. A. Seliga (1984), Radar Polarimetric Backscattering Properties of Conical Graupel, *Journal of the Atmospheric Sciences*, *41*(11), 1887–1892, doi:10.1175/1520-0469(1984)041<1887:rpbpoc>2.0.co;2.

Bailey, M. P., and J. Hallett (2009), A Comprehensive Habit Diagram for Atmospheric Ice Crystals: Confirmation from the Laboratory, AIRS II, and Other Field Studies, *Journal of the Atmospheric Sciences*, *66*(9), 2888–2899, doi:10.1175/2009jas2883.1.

Baran, A. J., P. Connolly, and C. Lee (2009), Testing an ensemble model of cirrus ice crystals using midlatitude in situ estimates of ice water content, volume extinction coefficient and the total solar optical depth, *Journal of Quantitative Spectroscopy and Radiative Transfer*, *110*(14-16), 1579–1598, doi:10.1016/j.jqsrt.2009.02.021.

Bechini, R., L. Baldini, and V. Chandrasekar (2013), Polarimetric Radar Observations in the Ice Region of Precipitating Clouds at C-Band and X-Band Radar Frequencies, *Journal of Applied Meteorology and Climatology*, *52*(5), 1147–1169, doi:10.1175/jamc-d-12-055.1.

Boucher O., et al. (2013), Clouds and Aerosols, *Climate Change 2013 - The Physical Science Basis*, 571–658, doi:10.1017/cbo9781107415324.016.

Brath, M., R. Ekelund, P. Eriksson, O. Lemke, and S. A. Buehler (2019), Microwave and submillimeter wave scattering of oriented ice particles, , doi:10.5194/amt-2019-382.

Bringi, V. N., and V. Chandrasekar (2005), *Polarimetric Doppler weather radar: principles and applications*, Cambridge University Press, Cambridge.

Brown, P. R. A., and P. N. Francis (1995), Improved Measurements of the Ice Water Content in Cirrus Using a Total-Water Probe, *Journal of Atmospheric and Oceanic Technology*, *12*(2), 410–414, doi:10.1175/1520-0426(1995)012<0410:imotiw>2.0.co;2.

Cantrell, W., and A. Heymsfield (2005), Production of Ice in Tropospheric Clouds: A Review, *Bulletin of the American Meteorological Society*, *86*(6), 795–808, doi:10.1175/bams-86-6-795.

Delanoë, J. (2005), Statistical properties of the normalized ice particle size distribution, *Journal of Geophysical Research*, *110*(D10), doi:10.1029/2004jd005405.

Delanoë, J. M. E., A. J. Heymsfield, A. Protat, A. Bansemer, and R. J. Hogan (2014), Normalized particle size distribution for remote sensing application, *Journal of Geophysical Research: Atmospheres*, *119*(7), 4204–4227, doi:10.1002/2013jd020700.

Demott, P. J. et al. (2011), Resurgence in Ice Nuclei Measurement Research, *Bulletin of the American Meteorological Society*, *92*(12), 1623–1635, doi:10.1175/2011bams3119.1.

DeMott, P. J., A. J. Prenni, X. Liu, S. M. Kreidenweis, M. D. Petters, C. H. Twohy, M. S. Richardson, T. Eidhammer, and D. C. Rogers (2010), Predicting global atmospheric ice nuclei distributions and their impacts on climate, *Proceedings of the National Academy of Sciences*, *107*(25), 11217–11222, doi:10.1073/pnas.0910818107.

Dolan, B., S. A. Rutledge, S. Lim, V. Chandrasekar, and M. Thurai (2013), A Robust C-Band Hydrometeor Identification Algorithm and Application to a Long-Term Polarimetric Radar Dataset, *Journal of Applied Meteorology and Climatology*, *52*(9), 2162–2186, doi:10.1175/jamc-d-12-0275.1.

Erfani, E., and D. L. Mitchell (2017), Growth of ice particle mass and projected area during riming, *Atmospheric Chemistry and Physics*, *17*(2), 1241–1257, doi:10.5194/acp-17-1241-2017.

Eriksson, P., R. Ekelund, J. Mendrok, M. Brath, O. Lemke, and S. A. Buehler (2018), A general database of hydrometeor single scattering properties at microwave and sub-millimetre wavelengths, *Earth System Science Data*, *10*(3), 1301–1326, doi:10.5194/essd-10-1301-2018.

Evensen, G. (1994), Sequential data assimilation with a nonlinear quasi-geostrophic model using Monte Carlo methods to forecast error statistics, *Journal of Geophysical Research*, *99*(C5), 10143, doi:10.1029/94jc00572.

Field, P. R. et al. (2016), Chapter 7. Secondary Ice Production - current state of the science and recommendations for the future, *Meteorological Monographs*, doi:10.1175/amsmonographs-d-16-0014.1.

Field, P. R., and A. J. Heymsfield (2015), Importance of snow to global precipitation, *Geophysical Research Letters*, *42*(21), 9512–9520, doi:10.1002/2015gl065497.

Field, P. R., R. J. Hogan, P. R. A. Brown, A. J. Illingworth, T. W. Choularton, and R. J. Cotton (2005), Parametrization of ice-particle size distributions for mid-latitude stratiform cloud, *Quarterly Journal of the Royal Meteorological Society*, *131*(609), 1997–2017, doi:10.1256/qj.04.134.

Fielding, M. D., J. C. Chiu, R. J. Hogan, and G. Feingold (2014), A novel ensemble method for retrieving properties of warm cloud in 3-D using ground-based scanning radar and zenith radiances, *Journal of Geophysical Research: Atmospheres*, *119*(18), doi:10.1002/2014jd021742.

Fielding, M. D., J. C. Chiu, R. J. Hogan, G. Feingold, E. Eloranta, E. J. O'connor, and M. P. Cadeddu (2015), Joint retrievals of cloud and drizzle in marine boundary layer clouds using ground-based radar, lidar and zenith radiances, *Atmospheric Measurement Techniques*, *8*(7), 2663–2683, doi:10.5194/amt-8-2663-2015.

Fusina, F., P. Spichtinger, and U. Lohmann (2007), Impact of ice supersaturated regions and thin cirrus on radiation in the midlatitudes, *Journal of Geophysical Research*, *112*(D24), doi:10.1029/2007jd008449.

Garrett, T. J., S. E. Yuter, C. Fallgatter, K. Shkurko, S. R. Rhodes, and J. L. Endries (2015), Orientations and aspect ratios of falling snow, *Geophysical Research Letters*, *42*(11), 4617–4622, doi:10.1002/2015gl064040.

Glienke, S., and F. Mei (2020), High-Volume Precipitation Spectrometer (HVPS) Instrument Handbook, doi:10.2172/1597643.

Grazioli, J., G. Lloyd, L. Panziera, C. R. Hoyle, P. J. Connolly, J. Henneberger, and A. Berne (2015), Polarimetric radar and in situ observations of riming and snowfall microphysics during CLACE 2014, *Atmospheric Chemistry and Physics*, *15*(23), 13787–13802, doi:10.5194/acp-15-13787-2015.

Gryspeerdt, E., O. Sourdeval, J. Quaas, J. Delanoë, M. Krämer, and P. Kühne (2018), Ice crystal number concentration estimates from lidar–radar satellite remote sensing – Part 2: Controls on the ice crystal number concentration, *Atmospheric Chemistry and Physics*, *18*(19), 14351–14370, doi:10.5194/acp-18-14351-2018.

Gu, Y., and D. S. Oliver (2007), An Iterative Ensemble Kalman Filter for Multiphase Fluid Flow Data Assimilation, *SPE Journal*, *12*(04), 438–446, doi:10.2118/108438-pa.

Gultepe, I., A. J. Heymsfield, P. R. Field, and D. Axisa (2017), Ice-Phase Precipitation, *Meteorological Monographs*, *58*, doi:10.1175/amsmonographs-d-16-0013.1.

Heymsfield, A. J., C. Schmitt, A. Bansemer, and C. H. Twohy (2010), Improved Representation of Ice Particle Masses Based on Observations in Natural Clouds, *Journal of the Atmospheric Sciences*, *67*(10), 3303–3318, doi:10.1175/2010jas3507.1.

Hogan, R. J., P. R. Field, A. J. Illingworth, R. J. Cotton, and T. W. Choularton (2002), Properties of embedded convection in warm-frontal mixed-phase cloud from aircraft and polarimetric radar, *Quarterly Journal of the Royal Meteorological Society*, *128*(580), 451–476, doi:10.1256/003590002321042054.

Hogan, R. J., M. P. Mittermaier, and A. J. Illingworth (2006), The Retrieval of Ice Water Content from Radar Reflectivity Factor and Temperature and Its Use in Evaluating a Mesoscale Model, *Journal of Applied Meteorology and Climatology*, *45*(2), 301–317, doi:10.1175/jam2340.1.

Hong, G., P. Yang, B. A. Baum, A. J. Heymsfield, F. Weng, Q. Liu, G. Heygster, and S. A. Buehler (2009), Scattering database in the millimeter and submillimeter wave range of 100–1000 GHz for nonspherical ice particles, *Journal of Geophysical Research*, *114*(D6), doi:10.1029/2008jd010451.

Hubbert, J. C., S. M. Ellis, W.-Y. Chang, S. Rutledge, and M. Dixon (2014), Modeling and Interpretation of S-Band Ice Crystal Depolarization Signatures from Data Obtained by Simultaneously Transmitting Horizontally and Vertically Polarized Fields, *Journal of Applied Meteorology and Climatology*, *53*(6), 1659–1677, doi:10.1175/jamc-d-13-0158.1.

Jiang, Z., M. Oue, J. Verlinde, E. E. Clothiaux, K. Aydin, G. Botta, and Y. Lu (2017), What Can We Conclude about the Real Aspect Ratios of Ice Particle Aggregates from Two-Dimensional Images?, *Journal of Applied Meteorology and Climatology*, *56*(3), 725–734, doi:10.1175/jamc-d-16-0248.1.

Jung, Y., M. Xue, and G. Zhang (2010), Simulations of Polarimetric Radar Signatures of a Supercell Storm Using a Two-Moment Bulk Microphysics Scheme, *Journal of Applied Meteorology and Climatology*, *49*(1), 146–163, doi:10.1175/2009jamc2178.1.

Kanji, Z. A., L. A. Ladino, H. Wex, Y. Boose, M. Burkert-Kohn, D. J. Cziczo, and M. Krämer (2017), Overview of Ice Nucleating Particles, *Meteorological Monographs*, *58*, doi:10.1175/amsmonographs-d-16-0006.1.

Keat, W. J., and C. D. Westbrook (2017), Revealing Layers of Pristine Oriented Crystals Embedded Within Deep Ice Clouds Using Differential Reflectivity and the Copolar Correlation Coefficient, *Journal of Geophysical Research: Atmospheres*, *122*(21), doi:10.1002/2017jd026754.

Keat, W. J., C. D. Westbrook, and A. J. Illingworth (2016), High-Precision Measurements of the Copolar Correlation Coefficient: Non-Gaussian Errors and Retrieval of the Dispersion Parameter μ in Rainfall, *Journal of Applied Meteorology and Climatology*, *55*(7), 1615–1632, doi:10.1175/jamc-d-15-0272.1.

Kennedy, P. C., and S. A. Rutledge (2011), S-Band Dual-Polarization Radar Observations of Winter Storms, *Journal of Applied Meteorology and Climatology*, *50*(4), 844–858, doi:10.1175/2010jamc2558.1.

Kollias, P., N. Bharadwaj, K. Widener, I. Jo, and K. Johnson (2014), Scanning ARM Cloud Radars. Part I: Operational Sampling Strategies, *Journal of Atmospheric and Oceanic Technology*, *31*(3), 569–582, doi:10.1175/jtech-d-13-00044.1.

Korolev, A. V., E. F. Emery, J. W. Strapp, S. G. Cober, G. A. Isaac, M. Wasey, and D. Marcotte (2011), Small Ice Particles in Tropospheric Clouds: Fact or Artifact? Airborne Icing Instrumentation Evaluation Experiment, *Bulletin of the American Meteorological Society*, *92*(8), 967–973, doi:10.1175/2010bams3141.1.

Korolev, A. V., J. W. Strapp, G. A. Isaac, and A. N. Nevzorov (1998), The Nevzorov Airborne Hot-Wire LWC–TWC Probe: Principle of Operation and Performance Characteristics, *Journal of Atmospheric and Oceanic Technology*, *15*(6), 1495–1510, doi:10.1175/1520-0426(1998)015<1495:tnahwl>2.0.co;2.

Korolev, A., J. W. Strapp, G. A. Isaac, and E. Emery (2013), Improved Airborne Hot-Wire Measurements of Ice Water Content in Clouds, *Journal of Atmospheric and Oceanic Technology*, *30*(9), 2121–2131, doi:10.1175/jtech-d-13-00007.1.

Kumjian, M. (2013), Principles and applications of dual-polarization weather radar. Part I: Description of the polarimetric radar variables, *Journal of Operational Meteorology*, *1*(19), 226–242, doi:10.15191/nwajom.2013.0119.

Kumjian, M. R., S. A. Rutledge, R. M. Rasmussen, P. C. Kennedy, and M. Dixon (2014), High-Resolution Polarimetric Radar Observations of Snow-Generating Cells, *Journal of Applied Meteorology and Climatology*, *53*(6), 1636–1658, doi:10.1175/jamc-d-13-0312.1.

Kuo, K.-S., W. S. Olson, B. T. Johnson, M. Grecu, L. Tian, T. L. Clune, B. H. V. Aartsen, A. J. Heymsfield, L. Liao, and R. Meneghini (2016), The Microwave Radiative Properties of Falling Snow Derived from Nonspherical Ice Particle Models. Part I: An Extensive Database of Simulated Pristine Crystals and Aggregate Particles, and Their Scattering Properties, *Journal of Applied Meteorology and Climatology*, *55*(3), 691–708, doi:10.1175/jamc-d-15-0130.1.

Leeuwen, P. J. V., and G. Evensen (1996), Data Assimilation and Inverse Methods in Terms of a Probabilistic Formulation, *Monthly Weather Review*, *124*(12), 2898–2913, doi:10.1175/1520-0493(1996)124<2898:daaimi>2.0.co;2.

Lindsey, D. T., and M. Fromm (2008), Evidence of the cloud lifetime effect from wildfire-induced thunderstorms, *Geophysical Research Letters*, *35*(22), doi:10.1029/2008gl035680.

Liu, G. (2008), A Database of Microwave Single-Scattering Properties for Nonspherical Ice Particles, *Bulletin of the American Meteorological Society*, *89*(10), 1563–1570, doi:10.1175/2008bams2486.1.

Lu, Y., Z. Jiang, K. Aydin, J. Verlinde, E. E. Clothiaux, and G. Botta (2016), A polarimetric scattering database for non-spherical ice particles at microwave wavelengths, *Atmospheric Measurement Techniques*, *9*(10), 5119–5134, doi:10.5194/amt-9-5119-2016.

Mace, G., and S. Benson (2017), Diagnosing Cloud Microphysical Process Information from Remote Sensing Measurements—A Feasibility Study Using Aircraft Data. Part I: Tropical Anvils Measured during TC4, *Journal of Applied Meteorology and Climatology*, *56*(3), 633–649, doi:10.1175/jamc-d-16-0083.1.

Mace, G. G., Q. Zhang, M. Vaughan, R. Marchand, G. Stephens, C. Trepte, and D. Winker (2009), A description of hydrometeor layer occurrence statistics derived from the first year of merged Cloudsat and CALIPSO data, *Journal of Geophysical Research*, *114*, doi:10.1029/2007jd009755.

Magono, C. (1962), Meteorological Classification of Snow Crystals, *Journal of the Japanese Society of Snow and Ice*, *24*(2), 33–37, doi:10.5331/seppyo.24.33.

Matrosov, S., A. Ryzhkov, J. Hardin, M. Shupe, M. Maahn, G. de Boer, and T. Uttal (2019), Intercomparisons of CloudSat and ground-based radar measurements during satellite overpasses, Available from: https://cscenter.co.jp/icrm2019/program/data/abstracts/Session11A-02_1.pdf (Accessed 17 October 2020)

Matsui, T., B. Dolan, S. A. Rutledge, W. K. Tao, T. Iguchi, J. Barnum, and S. E. Lang (2019), POLARRIS: A POLArimetric Radar Retrieval and Instrument Simulator, *Journal of Geophysical Research: Atmospheres*, *124*(8), 4634–4657, doi:10.1029/2018jd028317.

Mcfarquhar, G. M., T.-L. Hsieh, M. Freer, J. Mascio, and B. F. Jewett (2015), The Characterization of Ice Hydrometeor Gamma Size Distributions as Volumes in N0–λ–μ Phase Space: Implications for Microphysical Process Modeling, *Journal of the Atmospheric Sciences*, *72*(2), 892–909, doi:10.1175/jas-d-14-0011.1.

Mitchell, D. L. (1996), Use of Mass- and Area-Dimensional Power Laws for Determining Precipitation Particle Terminal Velocities, *Journal of the Atmospheric Sciences*, *53*(12), 1710–1723, doi:10.1175/1520-0469(1996)053<1710:uomaad>2.0.co;2.

Moisseev, D. N., S. Lautaportti, J. Tyynela, and S. Lim (2015), Dual-polarization radar signatures in snowstorms: Role of snowflake aggregation, *Journal of Geophysical Research: Atmospheres*, *120*(24), 12644–12655, doi:10.1002/2015jd023884.

Moisseev, D., A. V. Lerber, and J. Tiira (2017), Quantifying the effect of riming on snowfall using ground-based observations, *Journal of Geophysical Research: Atmospheres*, *122*(7), 4019–4037, doi:10.1002/2016jd026272.

Murphy, A. M., A. Ryzhkov, and P. Zhang (2020), Columnar Vertical Profile (CVP) Methodology for Validating Polarimetric Radar Retrievals in Ice Using In Situ Aircraft Measurements, *Journal of Atmospheric and Oceanic Technology*, *37*(9), 1623–1642, doi:10.1175/jtech-d-20-0011.1.

III Neely, R. R. et al. (2018), The NCAS mobile dual-polarisation Doppler X-band weather radar (NXPol), *Atmospheric Measurement Techniques*, *11*(12), 6481–6494, doi:10.5194/amt-11-6481-2018.

Newman, A. J., P. A. Kucera, and L. F. Bliven (2009), Presenting the Snowflake Video Imager (SVI), *Journal of Atmospheric and Oceanic Technology*, *26*(2), 167–179, doi:10.1175/2008jtecha1148.1.

Oue, M., M. Galletti, J. Verlinde, A. Ryzhkov, and Y. Lu (2016), Use of X-Band Differential Reflectivity Measurements to Study Shallow Arctic Mixed-Phase Clouds, *Journal of Applied Meteorology and Climatology*, *55*(2), 403–424, doi:10.1175/jamc-d-15-0168.1.

Oue, M., M. R. Kumjian, Y. Lu, Z. Jiang, E. E. Clothiaux, J. Verlinde, and K. Aydin (2015), X-Band Polarimetric and Ka-Band Doppler Spectral Radar Observations of a Graupel-Producing Arctic Mixed-Phase Cloud, *Journal of Applied Meteorology and Climatology*, *54*(6), 1335–1351, doi:10.1175/jamc-d-14-0315.1.

Oue, M., P. Kollias, A. Ryzhkov, and E. P. Luke (2018), Toward Exploring the Synergy Between Cloud Radar Polarimetry and Doppler Spectral Analysis in Deep Cold Precipitating Systems in the Arctic, *Journal of Geophysical Research: Atmospheres*, *123*(5), 2797–2815, doi:10.1002/2017jd027717.

Petäjä, T. et al. (2016), Biogenic Aerosols—Effects on Clouds and Climate (BAECC) Final Campaign Summary, , doi:10.2172/1242990.

Phillips, V. T. J., S. Patade, J. Gutierrez, and A. Bansemer (2018), Secondary Ice Production by Fragmentation of Freezing Drops: Formulation and Theory, *Journal of the Atmospheric Sciences*, *75*(9), 3031–3070, doi:10.1175/jas-d-17-0190.1.

Protat, A., J. Delanoë, D. Bouniol, A. J. Heymsfield, A. Bansemer, and P. Brown (2007), Evaluation of Ice Water Content Retrievals from Cloud Radar Reflectivity and Temperature Using a Large Airborne In Situ Microphysical Database, *Journal of Applied Meteorology and Climatology*, *46*(5), 557–572, doi:10.1175/jam2488.1.

Pruppacher, H. R., and J. D. Klett (1997), *Microphysics of clouds and precipitation*, Kluwer Acad. Publ., Dordrecht.

Ryzhkov, A. V., and D. S. Zrnic (2019), Polarimetric Microphysical Retrievals, *Springer Atmospheric Sciences Radar Polarimetry for Weather Observations*, 435–464, doi:10.1007/978-3-030-05093-1_11.

Ryzhkov, A., M. Pinsky, A. Pokrovsky, and A. Khain (2011), Polarimetric Radar Observation Operator for a Cloud Model with Spectral Microphysics, *Journal of Applied Meteorology and Climatology*, *50*(4), 873–894, doi:10.1175/2010jamc2363.1.

Schneider, J. et al. (2020), The seasonal cycle of ice-nucleating particles linked to the abundance of biogenic aerosol in boreal forests, , doi:10.5194/acp-2020-683.

Schrom, R. S., and M. R. Kumjian (2016), Connecting Microphysical Processes in Colorado Winter Storms with Vertical Profiles of Radar Observations, *Journal of Applied Meteorology and Climatology*, *55*(8), 1771–1787, doi:10.1175/jamc-d-15-0338.1.

Seliga, T. A., V. N. Bringi, and H. H. Al-Khatib (1981), A Preliminary Study of Comparative Measurements of Rainfall Rate Using the Differential Reflectivity Radar Technique and a Raingage Network, *Journal of Applied Meteorology*, *20*(11), 1362–1368, doi:10.1175/1520-0450(1981)020<1362:apsocm>2.0.co;2.

Skofronick-Jackson, G., M. Kulie, L. Milani, S. J. Munchak, N. B. Wood, and V. Levizzani (2019), Satellite Estimation of Falling Snow: A Global Precipitation Measurement (GPM) Core Observatory Perspective, *Journal of Applied Meteorology and Climatology*, *58*(7), 1429–1448, doi:10.1175/jamc-d-18-0124.1.

Sourdeval, O., E. Gryspeerdt, M. Krämer, T. Goren, J. Delanoë, A. Afchine, F. Hemmer, and J. Quaas (2018), Ice crystal number concentration estimates from lidar–radar satellite remote sensing – Part 1: Method and evaluation, *Atmospheric Chemistry and Physics*, *18*(19), 14327–14350, doi:10.5194/acp-18-14327-2018.

Spek, A. L. J., C. M. H. Unal, D. N. Moisseev, H. W. J. Russchenberg, V. Chandrasekar, and Y. Dufournet (2008), A New Technique to Categorize and Retrieve the Microphysical Properties of Ice Particles above the Melting Layer Using Radar Dual-Polarization Spectral Analysis, *Journal of Atmospheric and Oceanic Technology*, *25*(3), 482–497, doi:10.1175/2007jtecha944.1.

Stephens, G. L. (2005), Cloud Feedbacks in the Climate System: A Critical Review, *Journal of Climate*, *18*(2), 237–273, doi:10.1175/jcli-3243.1.

Stephens, G. L., M. Wild, P. W. Stackhouse, T. L'Ecuyer, S. Kato, and D. S. Henderson (2012), The Global Character of the Flux of Downward Longwave Radiation, *Journal of Climate*, *25*(7), 2329–2340, doi:10.1175/jcli-d-11-00262.1.

Taylor, J. W. et al. (2015), Observations of cloud microphysics and ice formation during COPE, *Atmospheric Chemistry and Physics Discussions*, *15*(11), 16049–16110, doi:10.5194/acpd-15-16049-2015.

Testud, J., S. Oury, R. A. Black, P. Amayenc, and X. Dou (2001), The Concept of "Normalized" Distribution to Describe Raindrop Spectra: A Tool for Cloud Physics and Cloud Remote Sensing, *Journal of Applied Meteorology*, *40*(6), 1118–1140, doi:10.1175/1520-0450(2001)040<1118:tcondt>2.0.co;2.

Tiira, J., and D. Moisseev (2020), Unsupervised classification of vertical profiles of dual polarization radar variables, *Atmospheric Measurement Techniques*, *13*(3), 1227–1241, doi:10.5194/amt-13-1227-2020.

Tiira, J., D. N. Moisseev, A. V. Lerber, D. Ori, A. Tokay, L. F. Bliven, and W. Petersen (2016), Ensemble mean density and its connection to other microphysical properties of falling snow as observed in Southern Finland, *Atmospheric Measurement Techniques*, *9*(9), 4825–4841, doi:10.5194/amt-9-4825-2016.

Tobo, Y., A. J. Prenni, P. J. DeMott, J. A. Huffman, C. S. Mccluskey, G. Tian, C. Pöhlker, U. Pöschl, and S. M. Kreidenweis (2013), Biological aerosol particles as a key determinant of ice nuclei populations in a forest ecosystem, *Journal of Geophysical Research: Atmospheres*, *118*(17), doi:10.1002/jgrd.50801.

Virkkula, A., J. Backman, P. P. Aalto, M. Hulkkonen, L. Riuttanen, T. Nieminen, M. D. Maso, L. Sogacheva, G. D. Leeuw, and M. Kulmala (2011), Seasonal cycle, size dependencies, and source analyses of aerosol optical properties at the SMEAR II measurement station in Hyytiälä, Finland, *Atmospheric Chemistry and Physics*, *11*(9), 4445–4468, doi:10.5194/acp-11-4445-2011.

Vivekanandan, J., B. Martner, M. Politovich, and G. Zhang (1999), Retrieval of atmospheric liquid and ice characteristics using dual-wavelength radar observations, *IEEE Transactions on Geoscience and Remote Sensing*, *37*(5), 2325–2334, doi:10.1109/36.789629.

Von Lerber, A., D. Moisseev, L. F. Bliven, W. Petersen, A.-M. Harri, and V. Chandrasekar (2017), Microphysical Properties of Snow and Their Link to Ze–S Relations during BAECC 2014, *Journal of Applied Meteorology and Climatology*, *56*(6), 1561–1582, doi:10.1175/jamc-d-16-0379.1.

Wang, Y., and V. Chandrasekar (2009), Algorithm for Estimation of the Specific Differential Phase, *Journal of Atmospheric and Oceanic Technology*, *26*(12), 2565–2578, doi:10.1175/2009jtecha1358.1.

Westbrook, C. D. (2004), Universality in snowflake aggregation, *Geophysical Research Letters*, *31*(15), doi:10.1029/2004gl020363.

Westbrook, C. D., R. C. Ball, P. R. Field, and A. J. Heymsfield (2004), Theory of growth by differential sedimentation, with application to snowflake formation, *Physical Review E*, *70*(2), doi:10.1103/physreve.70.021403.

Westbrook, C. D., and A. J. Illingworth (2013), The formation of ice in a long-lived supercooled layer cloud, *Quarterly Journal of the Royal Meteorological Society*, *139*(677), 2209–2221, doi:10.1002/qj.2096.

Xu, Y.-L. (1995), Electromagnetic scattering by an aggregate of spheres, *Applied Optics*, *34*(21), 4573, doi:10.1364/ao.34.004573.

Yun, Y., and J. E. Penner (2012), Global model comparison of heterogeneous ice nucleation parameterizations in mixed phase clouds, *Journal of Geophysical Research: Atmospheres*, *117*(D7), doi:10.1029/2011jd016506.

Yurkin, M. A., and A. G. Hoekstra (2011), The discrete-dipole-approximation code ADDA: Capabilities and known limitations, *Journal of Quantitative Spectroscopy and Radiative Transfer*, *112*(13), 2234–2247, doi:10.1016/j.jqsrt.2011.01.031.